communications engineering

A Nature Portfolio journal

Article

https://doi.org/10.1038/s44172-025-00424-3

Magnetic localization and manipulation of locking synchronous motors

Michiel Richter [1], Lukas Masjosthusmann[1], Pavlo Makushko[2], Venkatasubramanian Kalpathy Venkiteswaran[1], Denys Makarov [2] ✉ & Sarthak Misra [1,3] ✉

Three-dimensional (3D) localization of magneto-surgical devices is essential for safe and efficient navigation. However, existing magnetic localization methods either limit device miniaturization due to internal sensors or require additional excitation fields and external sensor arrays. Herein, we formulate a localization method based on the special properties of rotating magnetic dipoles, which allow reconstruction of position and rotation axis from a single external tri-axial magnetometer. The rotating dipole is realized through a permanent magnet synchronous motor (PMSM) that can reversibly (un)lock using the heat-induced phase transition of a low melting point alloy. Sequential localization and manipulation is performed by an external mobile electromagnet equipped with a single eye-in-hand Hall effect sensor. We describe the PMSM's thermal and magnetic properties, formulate the governing localization equations, quantify and validate 3D tracking of PMSM pose trajectory, and demonstrate sequential localization and manipulation in a benchtop experiment.

Collaboration between localization and manipulation systems is important for safe and efficient deployment of magnetic continuum robots[1,2] during diagnostic and therapeutic interventions[3]. Recent clinical demonstrations have shown the potential of these robots to navigate tortuous environments under magnetic manipulation[4–7]. Meanwhile, traditionally large stationary manipulation systems[8,9] are being downsized for greater mobility and reduced floorspace, moving toward commercialization[10–13]. These systems generate targeted magnetic fields toward manipulation of robots in vivo, which is facilitated by localization systems that reconstruct relative three-dimensional (3D) position and orientation information essential for control[14,15]. In this regard, localization connects manipulation systems to microsurgical devices.

Conventional medical localization methods use technologies like stereo vision[14,16], biplane fluoroscopy[17,18], angulated C-arm fluoroscopy[19,20], ultrasound[21–24], or magnetic resonance imaging systems[25–27]. These methods are compatible with various types of microrobots and offer various spatial and temporal resolutions, penetration depths, and sizes of infrastructure[28]. However, closed-loop magnetic manipulation is challenging due to often unknown coordinate transformations between physically disconnected reference frames of imaging and magnetic manipulation systems[29].

Alternatively, low-field localization methods (here defined in the nano- to milli-Tesla range), enable the development of magnetic tracking and manipulation systems that are independent of conventional medical imaging technologies[30]. These methods rely on detecting magnetic fields and reconstructing the relative pose of the field source[31]. They typically involve external magnetic field sources combined with internal sensorized devices[32–34] or magneto-mechanical resonators with external magnetometer arrays[35,36].

Sensorized magnetic devices, often equipped with a single tri-axial magnetometer[37–40], can be localized relative to, and manipulated by, external field generating hardware[30,33]. However, device miniaturization is limited by the space required for the sensor and the need for a rigid magnet-sensor connection to prevent saturation and maintain a consistent local field[30]. Alternatively, resonators offer better miniaturization potential by using a single magnet for both localization and manipulation, but they require targeted excitation fields and external magnetometer arrays to measure oscillating fields[36]. Increasing numbers of stationary magnetometers are required to expand the localization workspace when physically decoupled from magnetic manipulation systems[41,42]. This solution may have practical limitations in clinical settings. Alternatively, integration of external eye-in-hand magnetometers attached to mobile magnetic field generating systems provides connected mobile localization and manipulation workspaces[43].

In this work, we demonstrate a localization and manipulation approach that combines the benefits of sensorized devices, magneto-mechanical resonators, and eye-in-hand magnetometers. These include minimizing the required number of magnetometers, generating alternating

[1]Surgical Robotics Laboratory, Department of Biomechanical Engineering, University of Twente, Enschede, The Netherlands. [2]Helmholtz-Zentrum Dresden-Rossendorf e.V., Institute of Ion Beam Physics and Materials Research, Dresden, Germany. [3]Surgical Robotics Laboratory, Department of Biomaterials and Biomedical Technology, University of Groningen and University Medical Centre Groningen, Groningen, The Netherlands. ✉e-mail: d.makarov@hzdr.de; s.misra@utwente.nl

fields in vivo, and integrating electromagnetic localization and manipulation workspaces. Our method is based on rotating magnetic dipoles, which produce fields with elliptically varying strength at any point in space[44]. These fields provide four possible solutions to the pose of a rotating field source, based on measurements from a single tri-axial magnetometer[32]. Herein, this ambiguity is resolved using a priori knowledge of a rotating dipole position, obtained with closed-loop position feedback. The reconstructed dipole pose may be used to inform targeted generation of magnetic fields by a manipulation system.

As the rotating dipole, a milli-scale permanent magnet synchronous motor (PMSM) is developed (Fig. 1a). The motor includes planar-coil inspired[45] electromagnetic stators and a permanent magnet rotor. A ferrofluid bearing is used as an antifriction mechanism and ensures concentricity of the rotor and stator (Supplementary Movie 1). This bearing is inspired from other small-scale linear[46] and rotary motors[47,48], as low-cost and complexity alternatives to dry-film lubricants[49], jewel bearings[50], or microball bearings[51].

In order to demonstrate localization and manipulation of PMSMs, we introduce a rotor locking mechanism to the PMSM (Fig. 1b). This mechanism is inspired from the thermal and reversible solid-liquid phase transition of low melting point alloys (LMPA)[52,53]. Here, the stators of the PMSM act as heat and field sources[54] to induce LMPA liquefying and rotor rotation, respectively. The unlocked rotor (localization mode) allows reconstruction of the PMSM pose by an external magnetometer; the locked rotor (manipulation mode) allows the PMSM to act as a static permanent magnet able to be manipulated by external fields.

The external field source comprises an electromagnetic coil[22] equipped with an eye-in-hand tri-axial Hall effect sensor, for iterative magnetic manipulation and localization of the PMSM, respectively (Fig. 1c). Similar to the PMSM, the external system exhibits mode-switching. In localization mode, with the electromagnet deactivated and sensor/PMSM active, rotating fields from the PMSM are used to reconstruct its pose and reposition the coil. In manipulation mode, with the electromagnet activated and sensor/PMSM deactivated, the PMSM is mechanically rotated and displaced for steering (Fig. 1d).

The fabrication process of the PMSM, the characterization of its thermal and magnetic properties, as well as the validation of the LMPA-based locking mechanism, are described. Governing equations are formulated for the localization of rotating magnetic dipoles with perpendicular axes of magnetization and rotation. Quantitative experiments evaluate

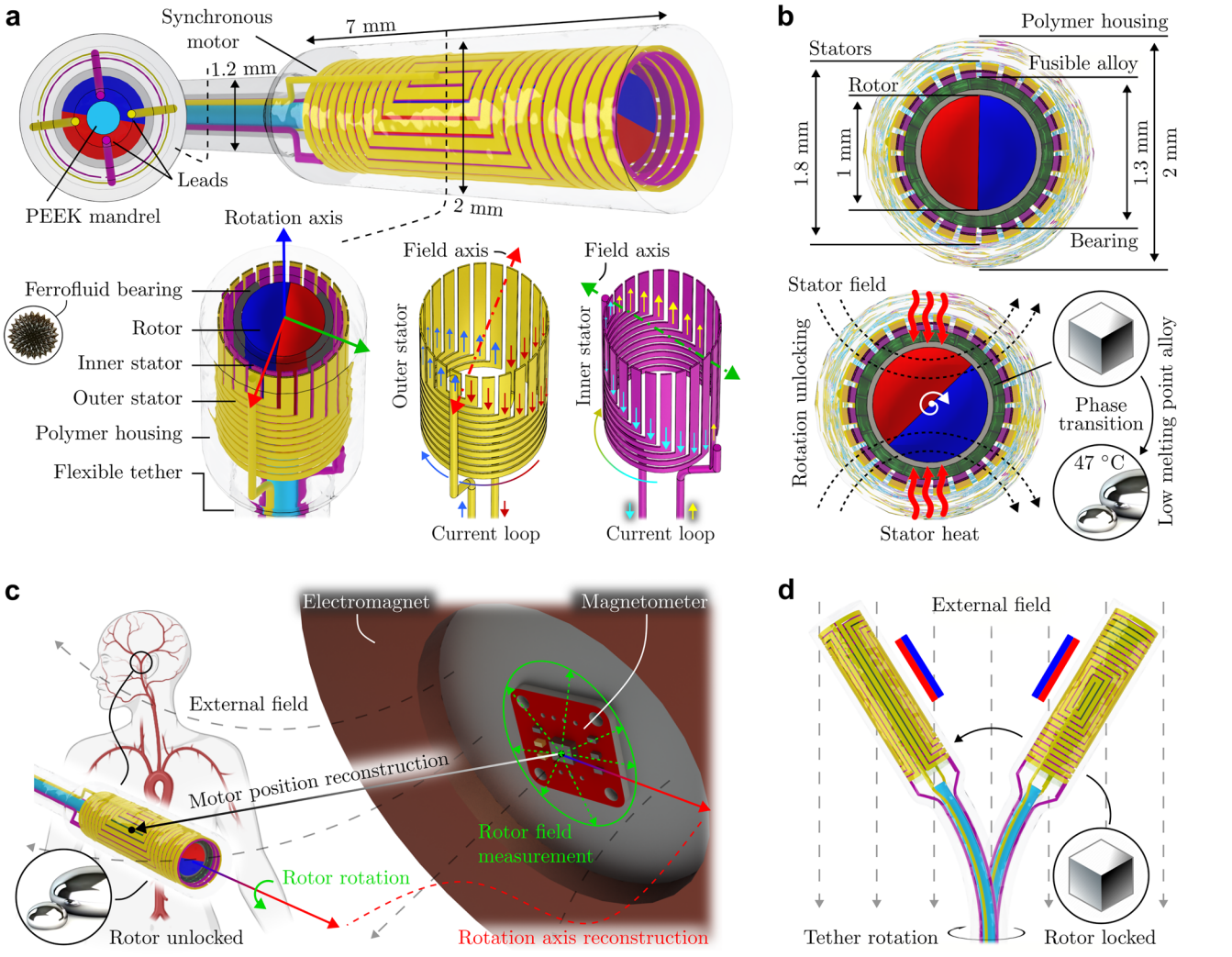

Fig. 1 | Schematic illustration of the permanent magnet synchronous motor (PMSM) for localization and manipulation. a Motor dimensions and components. The PMSM consists of two stators, which are made up of two planar coils wrapped cylindrically around a permanent magnetic rotor with a ferrofluid bearing. **b** A fusible low melting point alloy (LMPA) fills the rotor cavity and functions as a rotor locking mechanism. The heat and field produced by the stators simultaneously induce LMPA liquefying and rotor rotation, respectively. **c** The rotor generates a rotating magnetic field, which is detected by a single Hall effect sensor. These field measurements are used to determine the three-dimensional position and rotation axis of the motor. **d** When the LMPA solidifies, it locks the rotor in its orientation, enabling the motor to be steered in an external field by manually rotating the tether.

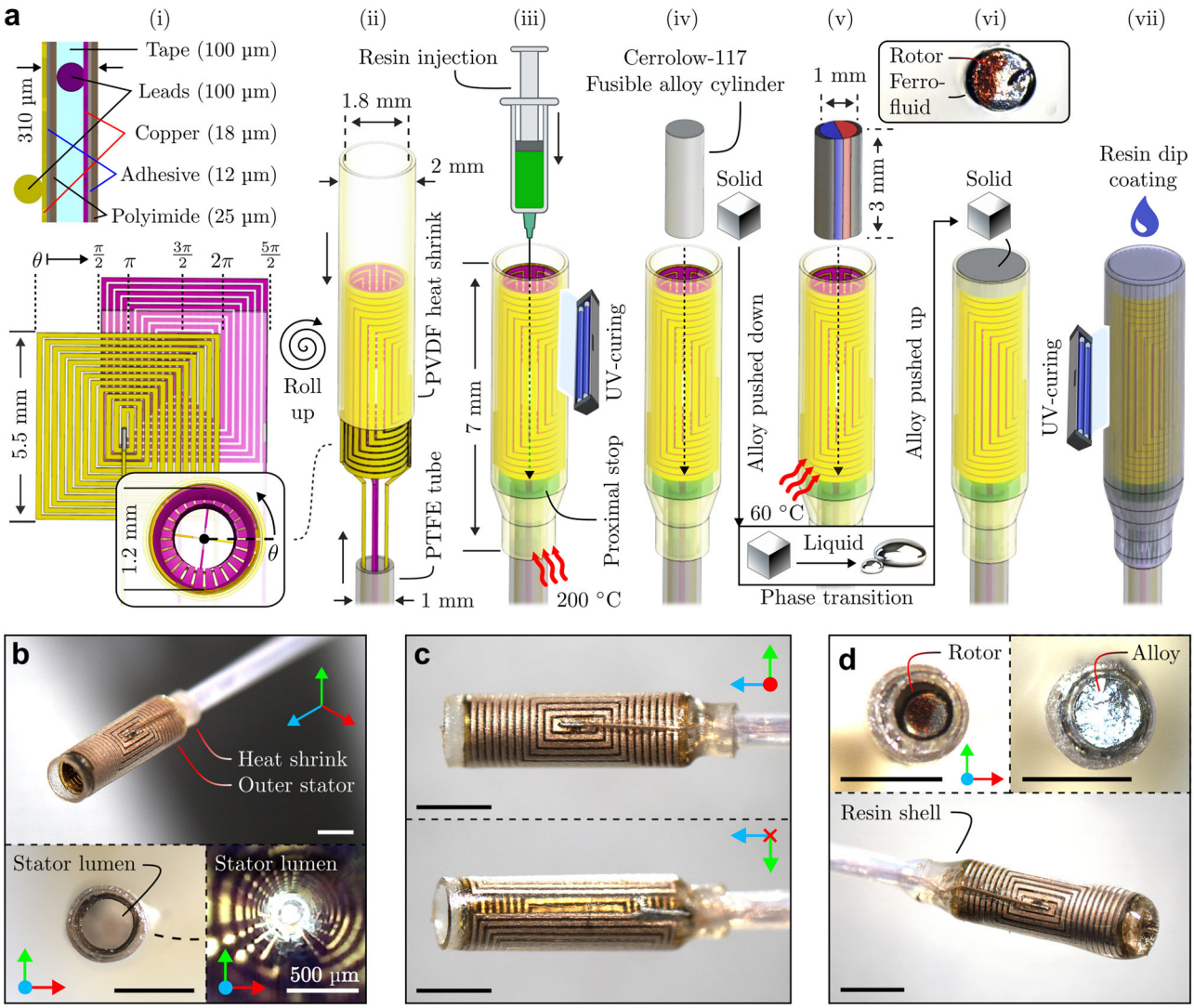

Fig. 2 | Permanent magnet synchronous motor (PMSM) components and assembly. a Fabrication of the PMSM. (i) Schematic of two stacked planar coils and a cross section with annotated dimensions. (ii) Planar coils are rolled into cylindrical stators with perpendicular angular orientation (θ). A PVDF tube maintains the shape and connects to a PTFE tube, guiding power leads. (iii) An injected low-friction resin seals the proximal opening of the stator lumen. (iv) The stator lumen is filled with a solid cylinder of Cerrolow 117 alloy. (v) The cylinder is molten, followed by inserting a diametrically magnetized rotor with a ferrofluid bearing. (vi) The liquid alloy is pushed up by inserting the magnet, and cooled to solidify. (vii) The motor is sealed with a resin dip coating. **b** Photographs of the stator structure and lumen. **c** Front and back views showing coil edge alignment when wrapped. **d** Top-view and isometric photographs of the stator lumen with the rotor and fusible alloy, and finished PMSM. Scale bar: 2 mm.

localization accuracy along 2D and 3D trajectories of the PMSM. Finally, a benchtop experiment demonstrates localization and manipulation of the PMSM in a tubular network, using an external integrated electromagnetic coil and eye-in-hand Hall effect sensor.

Results

Permanent magnet synchronous motor

Figure 2a illustrates the fabrication process and main components of the presented PMSM, comprising cylindrical stators made of two planar electromagnetic coils (Supplementary Fig. 1), a diametrically magnetized cylindrical rotor with ferrofluid bearing, an LMPA rotor lock, a polyvinylidene fluoride (PVDF) heat shrinkable tube stator holder, a polytetrafluoroethylene (PTFE) tether guiding power leads, and a resin shell/seal preventing LMPA leakage (cross-sectional views are provided in Supplementary Fig. 2).

Figure 2b shows the fabricated stator structure, including the PTFE tether, PVDF heat shrink, stators, and rotor cavity. A top view presents the cylindrical stator coils held by the PVDF tube, with the internal rotor cavity displaying the meandering copper strands of the coils. Figure 2c provides front and back side views of the stator. Meandering copper strands trace a cylindrical path and align at diametrically opposite positions, resulting in superposition of magnetic flux densities. Figure 2d depicts the rotor magnet inside the rotor cavity (north pole marked in red), the fusible alloy contained in the rotor cavity, and an isometric view of PMSM with the outer resin shell.

Motor properties

Stator magnetic field. A finite element model (FEM) of the stator structure simulates the electromagnetic field within the PMSM's rotor. In the stator coils, longitudinal copper strands generate a magnetic field in the diametric direction, while radial strands produce a field in the longitudinal direction. The magnetic field strength of the inner stator within the rotor volume ranges from 3 mT A^{-1} to 6 mT A^{-1} (Fig. 3a), assuming linearity between the generated field and electric current. Further, with quadrature sinusoidal currents through the inner and outer stator, average field strengths of 3.9 mT A^{-1} and 3.6 mT A^{-1} are achieved

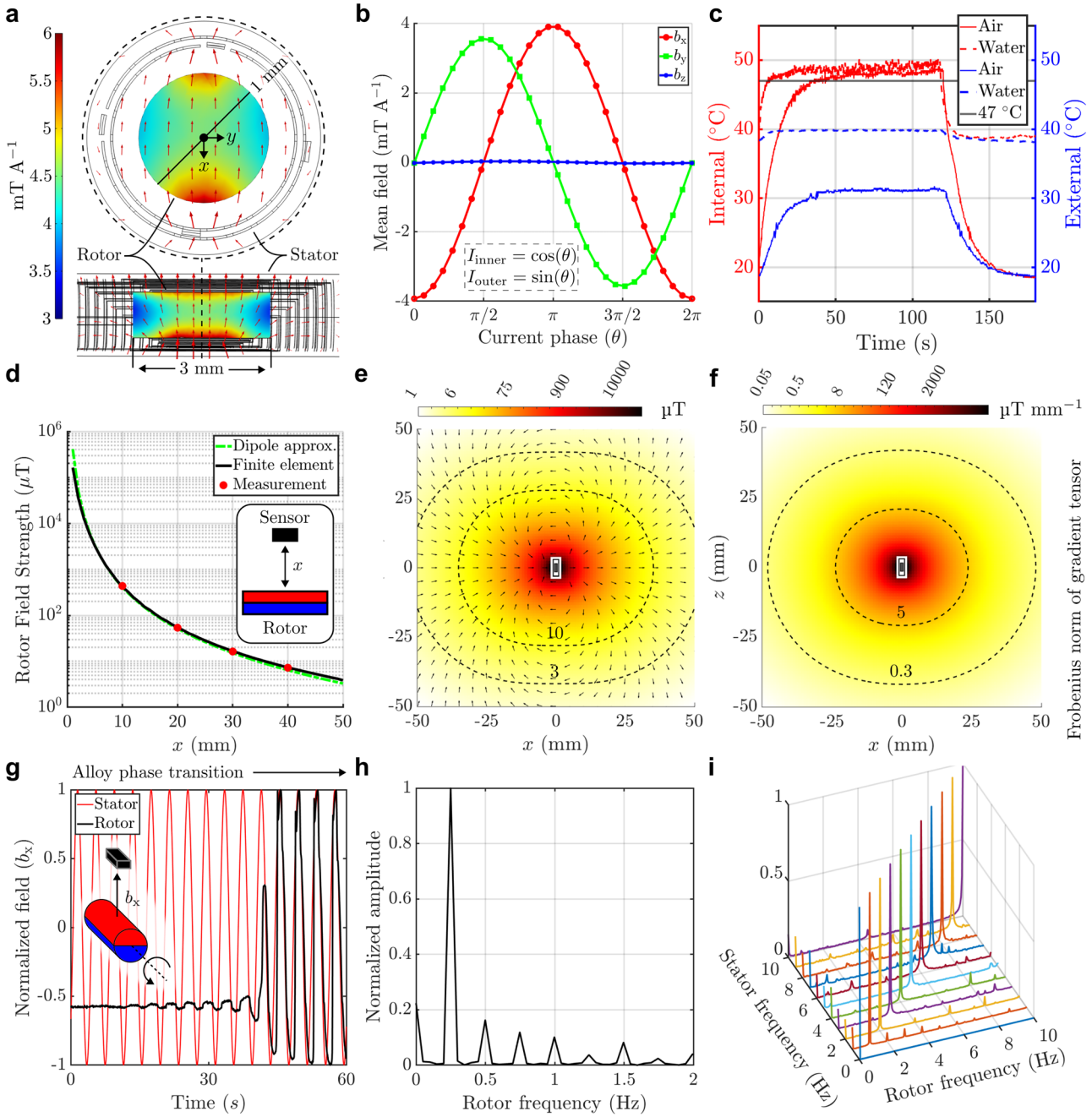

Fig. 3 | Characterization of magnetic, thermal, and frequency properties. **a**, **b** Simulated stator magnetic field ($\boldsymbol{b} = \langle b_x, b_y, b_z \rangle$) distribution in the rotor volume from quadrature unit-currents (I_{inner}, I_{outer}). **c** Measured internal and surface temperatures from 200 mA quadrature currents in room-temperature air (18 °C) and heated water (~37 °C). **d** Rotor field strength along its magnetization axis. **e**, **f** Field and gradient norms in the magnetization plane (magnetization and rotation axes). **g** Unlocking rotor rotation by phase transition of fusible alloy during stator activation. **h** Frequency analysis of rotor field signal during unlocked state. **i** Frequency analysis for motor frequencies up to 10 Hz, confirming synchronous rotation.

in perpendicular directions (Fig. 3b). The difference is due to the different inner diameters of the stators.

Stator heating. Temperature changes due to resistive heating and passive cooling of the stators, were measured at room temperature (18 °C) and in a bath of stationary heated water (~37 °C) using a thermocouple positioned internally or on the external surface (Supplementary Fig. 3). During heating, quadrature currents were applied to the inner ($I_{inner} = I \sin(2\pi f_m t)$) and outer stator coils ($I_{outer} = I \cos(2\pi f_m t)$) with current amplitude $I = 200$ mA and unit frequency ($f_m = 1$ Hz), over $t \in [0, 120]$ s. During cooling ($t \in [120, 180]$), currents were switched off. The quadrature current results in an electric power of $P = 0.165$ W, steady-state lumen temperatures of $T_{internal} \in \{49, 50\}$ °C, and PMSM surface temperatures of $T_{external} \in \{31, 40\}$ °C, in air and water, respectively (Fig. 3c).

Rotor magnetic field. The 3D magnetic field around the PMSM is modeled and scaled using field measurements from a Hall effect sensor (Fig. 3d–f). One-dimensional (1D) field measurements were taken by positioning the motor at varying distances ($x \in \{10, 20, 30, 40\}$ mm) above the sensor (Supplementary Fig. 4). The measured rotor field strengths ($b(x) \in \{411, 55, 18, 7\}$ μT) corresponds to the maximum field

strength where the rotor's magnetization axis is coincident with the sensor. These measurements were taken during rotor rotation. Static background fields and noise were averaged out during signal processing.

The 1D measurements are validated by comparison to a dipole approximation model, and thereafter used to scale a 3D finite element (FE) field model (Fig. 3d). This numerical FE model estimates magnetic fields around the rotor magnet. These estimates are used to fit an analytical 3D multipole expansion model (see "Materials and methods," $R^2 = 0.999$). Finally, this model and its spatial derivatives provide field strengths and gradients in the rotor's magnetization plane (Fig. 3e, f). We note that the general multipole expansion model may be interchanged for a simpler dipole approximation for modeling fields at sufficient distances from the rotor magnet[55].

Rotor locking alloy. The rotor locking mechanisms comprise a fusible alloy with a solid-liquid phase transition at 47 °C that melts due to resistive heating from the stators (Fig. 3g and Supplementary Movie 2).

Rotor unlocking is validated by positioning a Hall effect sensor above the motor, activating the stators with quadrature currents of $I = 175$ mA amplitude and $f_m = 0.25$ Hz frequency, and measuring the magnetic field over 60 s. During the phase transition ($t \in [0, 45]$ s), the rotor field varies sinusoidally with temporally increasing amplitude. Once fully liquefied ($t > 45$ s), the rotor rotation is synchronous with the stator field. The duration until complete phase transition is consistent with the temperature elevation corresponding to the amplitude of quadrature current (Fig. 3c).

Motor rotation frequency. The rotor's synchronous rotation at the set motor frequency ($f_m = 0.25$ Hz) is confirmed via frequency analysis of the field signal after liquefying of the alloy (Fig. 3h). Synchronous rotation is also validated across a range of frequencies ($f_m \in \{1, 2, \ldots, 10\}$ Hz), with the upper limit imposed by the maximum sampling frequency ($f_s = 20$ Hz) of the Hall effect sensor (Fig. 3i). In addition, a video recording shows rotor rotation up to a frequency of 10 Hz (Supplementary Movie 1).

Magnetic localization

The proposed localization method matches measured to modeled rotating field properties of the rotor within its magnetization plane. This plane is defined by the rotor's rotation axis ($\hat{\boldsymbol{\omega}}_m$) and magnetization axis ($\hat{\boldsymbol{\mu}}$), and contains 2D ellipse-shaped field isolines of uniform strength (Fig. 4a).

The 2D isolines are cross-sections of 3D tri-axial ellipsoids of constant field magnitude (b_{iso}), which rotate with the rotor by an angle (ϕ) about $\hat{\boldsymbol{\omega}}_m$ (Fig. 4c). The field ($\boldsymbol{b}(\boldsymbol{p}, \phi)$) at any position ($\boldsymbol{p} \in \mathbb{R}^3$) changes in strength and direction synchronous to ϕ. Maximum field strength occurs when $\boldsymbol{p}$ coincides with the smallest isoline in the magnetization plane ($b_{max} = \| \boldsymbol{b}(\boldsymbol{p}, \phi_{max}) \|$, where $\phi_{max} \in \{0, \pi\}$. Minimum field strength occurs at a quarter turn ($\phi_{min} \in \{\pi/2, 3\pi/2\}$). The ratio of maximum to minimum field strength defines the field ratio ($b_{ratio} = b_{max}/b_{min}$). Further, the field ($\boldsymbol{b}(\boldsymbol{p}, \phi)$) rotates within a plane around the field rotation axis ($\hat{\boldsymbol{\omega}}_b$) and forms an ellipse with principal axes $\{b_{max}, b_{min}\}$ (Supplementary Fig. 5).

These field properties apply to any position in space, which periodically coincides with an isoline in the magnetization plane. Therefore, field properties can be linked to isoline positions. Next, we formulate "rotor field isoline functions" to describe the relationship between rotating field properties and corresponding isoline positions.

Rotor field isoline functions. A 2D isoline in the rotor's magnetization plane is defined by field strength (b_{iso}) and position angle (β). We define an isoline position vector ($\boldsymbol{p}_e(b_{iso}, \beta)$) that traces the ellipse-shaped path, and that corresponds to a maximum field ($\boldsymbol{b}_{max}(\boldsymbol{p}_e)$), minimum field ($\boldsymbol{b}_{min}(\boldsymbol{p}_e)$), field rotation axis ($\hat{\boldsymbol{\omega}}_b(\boldsymbol{p}_e)$), field ratio ($b_{ratio}(\boldsymbol{p}_e) = \| \boldsymbol{b}_{max}(\boldsymbol{p}_e) \| / \| \boldsymbol{b}_{min}(\boldsymbol{p}_e) \|$), and field rotation angle ($\alpha(\boldsymbol{p}_e)$) between the field's rotation axis and the rotor's magnetization axis (Fig. 4d and Supplementary Fig. 5).

The rotor field isoline functions depend on (a subset of) isoline variables $\{b_{iso}, \beta\}$, and include position ($\boldsymbol{p}_e(b_{iso}, \beta)$), field ratio ($b_{ratio}(\beta)$), and field angle ($\alpha(\beta)$). These three isoline functions are formulated based on simulated values from the magnetic field model of the rotor. The isoline functions show that the isoline position distance ($\|\boldsymbol{p}_e(b_{iso}, \beta)\|$) varies elliptically along along each isoline (Fig. 4e). Also, $b_{ratio} \in [1, 2]$ is cyclic and bounded along each isoline (also see Supplementary Text 1), with four possible solutions for $\beta \in \{\beta_1, \pi - \beta_1, \pi + \beta_1, -\beta_1\}$, $\beta_1 \in [0, \pi/2]$ (Fig. 4f). Similarly, $\alpha(\beta) \in [0, \pi]$ is cyclic and bounded. In this work, the ambiguity of β is resolved by using a priori knowledge of rotor position through closed-loop feedback of previous localizations (Eq. 14 and Fig. 8d).

Notably, the magnetic field of the stators is ignored during the formulation of the isoline functions. Upon synchronous rotation of the rotor's magnetization axis with the stator field, we assume that the stator only acts to amplify the PMSM's magnetic moment. In that case, although the PMSM's field strengths ($\{b_{max}, b_{min}\}$, $b_* := \| \boldsymbol{b}_* \|$) shift for some $\boldsymbol{p}_e$, its $\{b_{ratio}, \hat{\boldsymbol{b}}_{min}, \hat{\boldsymbol{\omega}}_b\}$ does not. Since $\|\boldsymbol{p}_e\|$ depends on $b_{iso} \equiv b_{max}$, this is the only theoretically affected isoline function (Eq. 9). However, given the stator field's weakness compared to that of the rotor (Supplementary Fig. 6), its impact on $\{b_{max}, b_{min}\}$ is considered negligible.

Magnetic localization algorithm. Magnetic localization of the PMSM is informed by field measurements taken by a Hall effect sensor at some position in space around the PMSM. These measurements are used in the rotor field isoline functions to compute the sensor's isoline position in the rotor's magnetization plane. Then, the position and rotation axis of the PMSM are determined using both the measured field components and the reconstructed isoline parameters (Supplementary Fig. 7). Figure 5a shows the localization setup, with a Hall effect sensor and PMSM. The goal is to reconstruct the motor's position (${}^S\boldsymbol{p}_m$) and rotation axis (${}^S\boldsymbol{\omega}_m$) relative to the sensor frame ($\{S\}$).

Figure 5b illustrates field measurement post-processing. Temporal field measurements (${}^S\boldsymbol{b}(t)$) consist of the static Earth's field, rotating PMSM field, and sensor noise. The Earth's field is obtained through frequency analysis and subtracted from the measurement signal, giving the motor's field (${}^S\boldsymbol{b}_m(t)$). Then, a vector plot of ${}^S\boldsymbol{b}_m(t)$ shows formation of a 3D ellipse in the reference frame of the sensor (${}^S\boldsymbol{R} = [{}^S\hat{\boldsymbol{x}}, {}^S\hat{\boldsymbol{y}}, {}^S\hat{\boldsymbol{z}}]$), characterized by a normal vector equal to the field's rotation axis (${}^S\boldsymbol{\omega}_b$), and principal axes representing vectors of maximum (${}^S\boldsymbol{b}_{max}$) and minimum field strength (${}^S\boldsymbol{b}_{min}$). This additionally gives the field ratio (${}^S b_{ratio} = \| {}^S\boldsymbol{b}_{max} \| / \| {}^S\boldsymbol{b}_{min} \|$).

Figure 5c again visualizes ${}^S\boldsymbol{b}_m(t)$ in the sensor's reference frame, including the reconstructed ${}^S\boldsymbol{b}_{max}$, ${}^S\boldsymbol{b}_{min}$, and ${}^S\hat{\boldsymbol{\omega}}_b$. By definition, the rotor's magnetization plane is spanned by ${}^S\boldsymbol{b}_{max}$ and ${}^S\hat{\boldsymbol{\omega}}_b$. Therefore, ${}^S\hat{\boldsymbol{b}}_{min}$ is perpendicular to the magnetization plane. The vector of maximum field strength is coincident and parallel to the magnetization plane, and identifies the isoline field strength ($b_{iso} := \| {}^S\boldsymbol{b}_{max} \|$).

Figure 5d shows the method of matching field measurements to an isoline position in the magnetization plane, followed by reconstruction of the motor pose relative to the sensor. A non-unique isoline position angle (${}^S\beta \in \{{}^S\beta_1, {}^S\beta_2, {}^S\beta_3, {}^S\beta_4\}$) is computed by minimizing the difference between measured and modeled field ratios. This leads to an associated isoline position (${}^S\boldsymbol{p}_e(b_{iso}, {}^S\beta)$) and field angle (${}^S\alpha({}^S\beta)$). Finally, the relative motor position (${}^S\boldsymbol{p}_m$) and rotation axis (${}^S\hat{\boldsymbol{\omega}}_m$) are found by rotating the reconstructed field rotation axis (${}^S\hat{\boldsymbol{\omega}}_b$) around the perpendicular rotation vector (${}^S\hat{\boldsymbol{b}}_{min}\psi$) by a function of isoline angles ($\{{}^S\beta, {}^S\alpha\}$) scaled to coefficients ($c_1, c_2 \in \{-1, 1\}$). These combinations of coefficients represent the four possible solutions for ${}^S\beta$ and can be obtained through optimization based on a priori knowledge of motor position, or triangulation with an additional sensor.

Magnetic localization validation. Magnetic localization is validated by moving the PMSM relative to a fixed Hall effect sensor using a robotic arm (Supplementary Fig. 4 and Supplementary Movie 3). The PMSM is displaced such that the sensor traces field isoline positions ($\boldsymbol{p}_e(b_{iso}, \beta)$) of

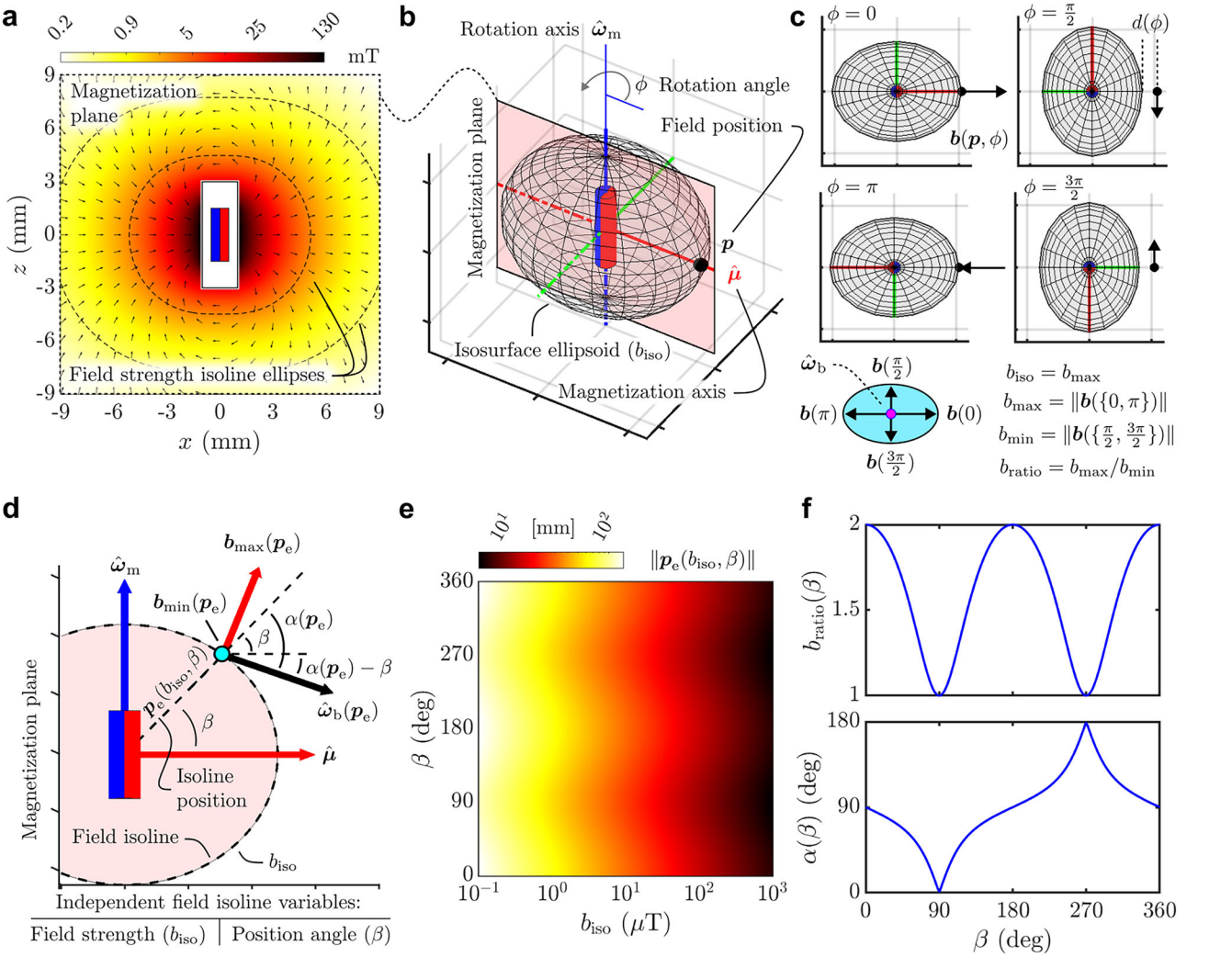

Fig. 4 | Formulation of rotor field isoline functions. a Magnetic field isolines and arrows in the rotor's magnetization plane (magnetization and rotation axes). **b** Field isolines are 2D cross-sections of tri-axial ellipsoidal field isosurfaces, which rotate about a motor rotation axis ($\hat{\omega}_m$) with an angle (ϕ) during activation. **c** In situ rotation of field ellipsoidal isosurfaces generates rotating fields ($\boldsymbol{b}(\boldsymbol{p}, \phi)$) at any position ($\boldsymbol{p}$), which itself forms an ellipse with principal axes defined by the maximum and minimum field strengths (b_{max}, b_{min}). **d** Schematic representation of the magnetization plane, with an isoline ellipse traced by a position ($\boldsymbol{p}_e(b_{iso}, \beta)$) defined by the isoline field strength (b_{iso}) and position angle (β) from the magnetization axis ($\hat{\boldsymbol{\mu}}$). Any isoline position ($\boldsymbol{p}_e$) is additionally associated with vectors of maximum field ($\boldsymbol{b}_{max}$), minimum field ($\boldsymbol{b}_{min}$), field rotation axis ($\hat{\boldsymbol{\omega}}_b$), and scalars of field ratio ($b_{ratio} = \| \boldsymbol{b}_{max} \| / \| \boldsymbol{b}_{min} \|$) and field angle ($\alpha := \angle\hat{\boldsymbol{\omega}}_b, \boldsymbol{p}_e$). A 3D representation is provided in Supplementary Fig. 5. **e** Analytical function fit to isoline position vectors ($\boldsymbol{p}_e(b_{iso}, \beta) : \mathbb{R}^2 \to \mathbb{R}^2$), showing distances from the rotor magnet to isoline positions. **f** Analytical function fit to field ratio ($b_{ratio}(\beta) : \mathbb{R} \to \mathbb{R}$) and field angle ($\alpha(\beta) : \mathbb{R} \to \mathbb{R}$), considering that $\alpha(\beta) = \alpha(b_{iso}, \beta) \equiv \alpha(\boldsymbol{p}_e)$.

chosen isoline field strength (b_{iso}) and position angle (β) in the motor frame (Fig. 6a and Supplementary Movie 3). Known motor-robot-sensor transformations give the associated reference motor position ($\boldsymbol{p}_m$) and rotation axis ($\hat{\boldsymbol{\omega}}_m$) relative to the sensor. At each $\boldsymbol{p}_e$, field measurement-based reconstruction of motor position (${}^S\boldsymbol{p}_m$) and rotation axis (${}^S\hat{\boldsymbol{\omega}}_m$) is performed (Fig. 6b). During localization, the PMSM is activated at a motor frequency of $f_m = 1$ Hz for 30 s, with field measurements taken at the upper limit of our sensor sampling frequency ($f_s = 20$ Hz).

Figure 6c shows localization results for isoline positions defined by various combinations of position angles ($\beta \in \{0, 7.5, 15, \ldots, 90\}°$) and field strengths ($b_{iso} \in \{6, 10, 20, 50, 100\}$ μT). The field strengths correspond to motor-sensor distances ($\| \boldsymbol{p}_m \| \leq 43$ mm. The tracing of isolines by the sensor is validated through the maximum measured motor field strength (Fig. 6c(i)). The weakest isoline field strength ($b_{iso} = 6$ μT) corresponds to the lower boundary of signal-to-noise ratio (SNR ≥ 10 dB) for which we obtained consistent localization results (Fig. 6c(ii)).

Sensor noise, measured to be between 2 and 4 μT (Supplementary Fig. 6), determines whether the maximum and minimum field strength can be reliably differentiated (Fig. 6c(iii)). For those positions where $\| \boldsymbol{b}_{max} - \boldsymbol{b}_{min} \| \geq 2\,\mu$T, errors in reconstructed field ratio are $|{}^S b_{ratio} - b_{ratio}| \leq 0.12$ (Fig. 6c(iv)). The error in ${}^S b_{ratio}$ determines the error in isoline position angle (Fig. 5d and Eq. 8) as $|{}^S\beta - \beta| \leq 23°$ (Fig. 6c(v)), and isoline field angle as $|{}^S\alpha - \alpha(\beta)| \leq 10°$ (Fig. 6c(vi)). Finally, localization accuracy in distance offset is $\|\boldsymbol{p}_m - {}^S\boldsymbol{p}_m\| \leq 7$ mm (Fig. 6c(vii)), and for directionality vectors of motor position $\angle\hat{\boldsymbol{p}}_m, {}^S\hat{\boldsymbol{p}}_m \leq 11°$ (Fig. 6c(viii)) and rotation axis $\angle\hat{\boldsymbol{\omega}}_m, {}^S\hat{\boldsymbol{\omega}}_m \leq 23°$ (Fig. 6c(ix)).

In order to analyze the angular errors in ${}^S\hat{\boldsymbol{p}}_m$ and ${}^S\hat{\boldsymbol{\omega}}_m$, consider that both equally depend on those in reconstructed field vectors ($\{{}^S\hat{\boldsymbol{b}}_{min}, {}^S\hat{\boldsymbol{\omega}}_b\}$), seen in the governing localization equations (Fig. 5d and Eqs. 11–13). Further, ${}^S\hat{\boldsymbol{p}}_m$ depends on ${}^S\alpha$, whereas ${}^S\hat{\boldsymbol{\omega}}_m$ depends on $\{{}^S\beta, {}^S\alpha\}$. Also, ${}^S\alpha$ depends on ${}^S\beta$, that depends on ${}^S b_{ratio}$. From the partial derivatives of the isoline parameters, we observe that $|\partial\alpha(\beta \leq 60°)/\partial\beta| \leq 1$ and mitigates errors in ${}^S\beta$, but amplifies above (Supplementary Fig. 8). This is seen from the peaks at $\beta = 23°$ and $\beta = 65°$ (Fig. 6c(v), (vi)). Also, $|\partial\beta/\partial b_{ratio}|$ and $|\partial\alpha/\partial b_{ratio}|$ are most sensitive to errors at the boundary of $b_{ratio}(\beta) \in \{1, 2\}$, and least-sensitive when $b_{ratio}(\beta) \in [1.1, 1.9]$. This corresponds to the relative motor-sensor configurations with isoline position angles of $\beta \in [25, 75]°$ (Fig. 4f).

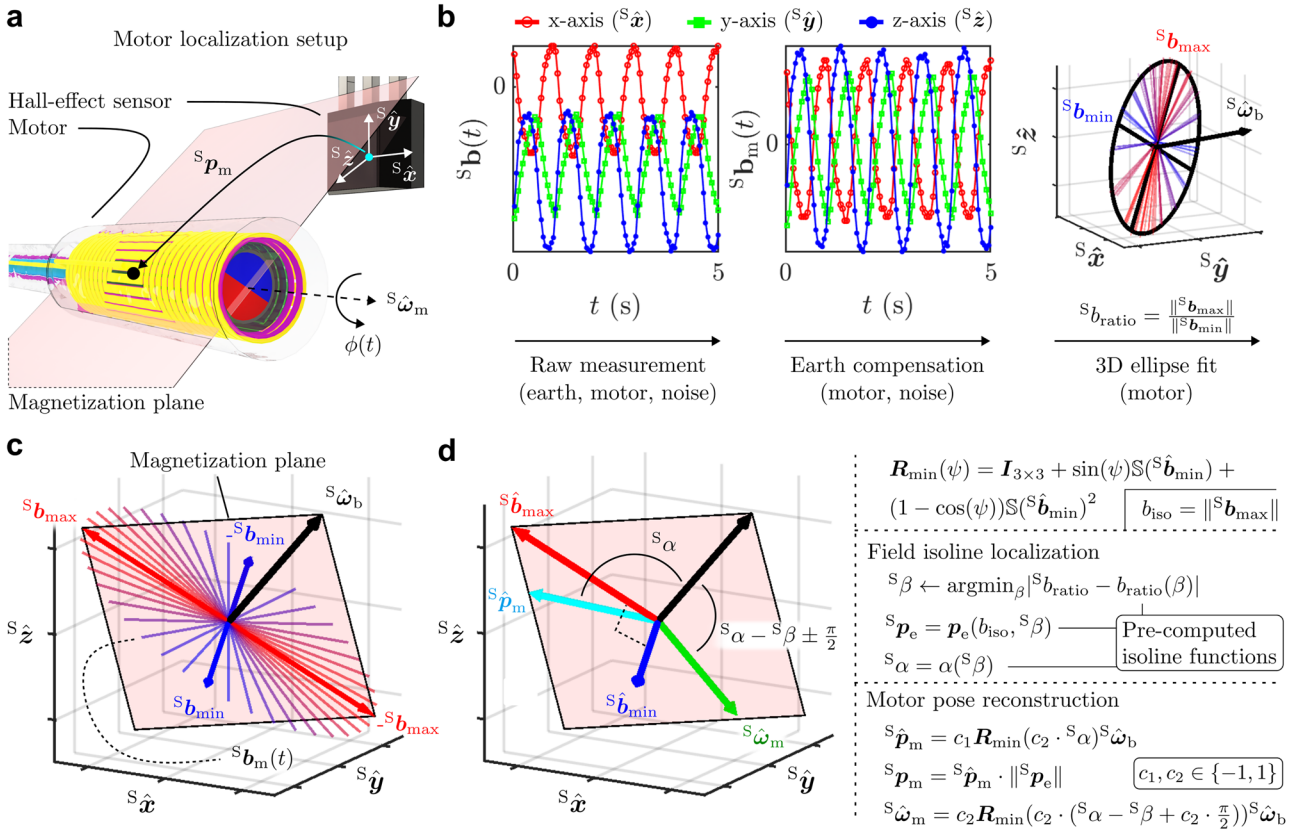

Fig. 5 | Schematic representation of the magnetic localization algorithm. a Setup with a Hall effect sensor and its local Cartesian axes ($\{{}^{S}\hat{\boldsymbol{x}}, {}^{S}\hat{\boldsymbol{y}}, {}^{S}\hat{\boldsymbol{z}}\}$), and motor with position (${}^{S}\boldsymbol{p}_m$) and rotation axis (${}^{S}\boldsymbol{\omega}_m$) relative to the sensor. **b** Temporal field measurements (${}^{S}\boldsymbol{b}(t)$) are compensated for the Earth's field to obtain the motor field signal (${}^{S}\boldsymbol{b}_m(t)$). This signal forms an ellipse with principal axes equal to vectors of maximum (${}^{S}\boldsymbol{b}_{max}$) and minimum strength (${}^{S}\boldsymbol{b}_{min}$), and a normal vector equal to the field's rotation axis (${}^{S}\hat{\boldsymbol{\omega}}_b$). **c** The rotor's magnetization plane is spanned by ${}^{S}\hat{\boldsymbol{b}}_{max}$ and ${}^{S}\hat{\boldsymbol{\omega}}_b$, with ${}^{S}\hat{\boldsymbol{b}}_{min}$ perpendicular. **d** A rotation matrix ($\boldsymbol{R}_{min}(\psi)$) associated with the rotation vector (${}^{S}\hat{\boldsymbol{b}}_{min}\psi$) is defined with $\mathbb{S}(*) : \mathbb{R}^3 \to \mathbb{R}^{3\times3}$ a skew-symmetric matrix. Isoline parameters are matched to the measured field ratio (${}^{S}b_{ratio}$), yielding solutions for the isoline position angle (${}^{S}\beta$), position vector (${}^{S}\boldsymbol{p}_e$), and field angle (${}^{S}\alpha$). These parameters are used to reconstruct the motor pose.

Angular errors in $\{{}^{S}\beta, {}^{S}\alpha, {}^{S}\hat{\boldsymbol{p}}_m, {}^{S}\hat{\boldsymbol{\omega}}_m\}$ expectedly to increase with β, for which $\| \boldsymbol{b}_{max} - \boldsymbol{b}_{min} \|$ falls below the sensor noise, and reconstructed components of the measured field become less accurate. Unexpectedly, however, the error $|{}^{S}\beta - \beta|$ increases linearly with $\beta \leq 23°$ (Fig. 6c(v)). This error stems from an overestimation of ${}^{S}b_{ratio} \approx 2, \quad \forall\beta \leq 23°$, which is observed for all field strengths and appears unrelated to the SNR (Fig. 6c(iv)). A potential cause is observed in $\partial(\| \boldsymbol{b}_{max} \| - \| \boldsymbol{b}_{min} \|)/\partial\beta \approx 0, \quad \forall\beta \leq 23°$ (Fig. 6c(iii)), that indicates a region where changes in relative maximum and minimum field strengths are indistinguishable from sensor noise.

Three-dimensional trajectory tracking

The three-dimensional tracking of motor pose is demonstrated along cubic (Fig. 7a), helical (Fig. 7b), and sinusoidal paths (Fig. 7c). Each trajectory consists of a series of predetermined positions ($\boldsymbol{p}_m = \langle p_{m,x}, p_{m,y}, p_{m,z} \rangle$) and rotation axes ($\hat{\boldsymbol{\omega}}_m$) with respect to the sensor. These poses are iteratively traced by the PMSM using a robotic arm (Fig. 6a and Supplementary Movie 3). At each iteration, the motor's position (${}^{S}\boldsymbol{p}_m$) and rotation axis (${}^{S}\hat{\boldsymbol{\omega}}_m$) are reconstructed. At the first iteration, the known motor position ($\boldsymbol{p}_m$) is used as the initial guess to compute ${}^{S}\boldsymbol{p}_m$. In subsequent iterations, the previously reconstructed ${}^{S}\boldsymbol{p}_m$ is used as feedback (Supplementary Fig. 7).

Figure 7 reports absolute sensor-to-motor distance ($\|\boldsymbol{p}_m\|$) along each trajectory, localization distance error ($\|\boldsymbol{p}_m - {}^{S}\boldsymbol{p}_m\|$), measured maximum field strength (${}^{S}b_{max} \equiv {}^{S}b_{iso}$), and reconstructed isoline position angle (${}^{S}\beta$). Additionally, for all isoline position angles (β) along each trajectory, the angular errors in position angle (${}^{S}\beta - \beta$), and PMSM directionality vectors for position ($\angle\boldsymbol{p}_m$, ${}^{S}\boldsymbol{p}_m$) and rotation axes ($\angle\hat{\boldsymbol{\omega}}_m$, ${}^{S}\hat{\boldsymbol{\omega}}_m$), are shown.

The tracking results support previous findings that localization is most accurate for $\beta \in [25, 75]°$ (Fig. 6). Angular errors in position vectors are found to be within $\angle\,\boldsymbol{p}_m, {}^{S}\boldsymbol{p}_m \in [5, 15]°$, whereas for rotation axis within $\angle\hat{\boldsymbol{\omega}}_m, {}^{S}\hat{\boldsymbol{\omega}}_m \in [10, 40]^\circ$. Localization errors increase for $\beta < 25°$, possibly due to a region of low sensor accuracy and precision.

Errors and standard deviations in $\angle\hat{\boldsymbol{\omega}}_m$, ${}^{S}\hat{\boldsymbol{\omega}}_m$ likely stem from incorrect optimization of the localization coefficients $\{c_1, c_2\}$ (Eq. 14). Figure 7 (central panels) shows abrupt deviations in the reconstructed position, indicating a series of faulty localizations. These errors persist due to feedback to subsequent localization iterations (Supplementary Fig. 7). Since $\{c_1, c_2\}$ are optimized based on prior positions, the position angular error ($\angle\,\boldsymbol{p}_m, {}^{S}\boldsymbol{p}_m$) changes less between iterations. However, an incorrect sign of $c_2 = \pm1$ already introduces a 90° error in ${}^{S}\hat{\boldsymbol{\omega}}_m$ (Eq. 13), with the potential for variation in angular errors ($\angle\hat{\boldsymbol{\omega}}_m$, ${}^{S}\hat{\boldsymbol{\omega}}_m$) between iterations.

Magnetic localization and manipulation

Iterative magnetic localization and manipulation of the PMSM is demonstrated in a 2D tubular network (Supplementary Fig. 9 and Supplementary Movie 4). The experimental setup includes an integrated external localization-manipulation system comprising a Hall effect sensor mounted on the tip of an electromagnet, serving as the end-effector of a serial manipulator (Fig. 8a). The external system is vertically positioned above the PMSM and enclosing tubular network, using field measurements from the sensor to track and follow the PMSM's movement (Fig. 8b).

The system alternates between localization and manipulation modes (Fig. 8c). In localization mode, the active PMSM generates a rotating field, while the Hall effect sensor takes temporal field measurements. In this

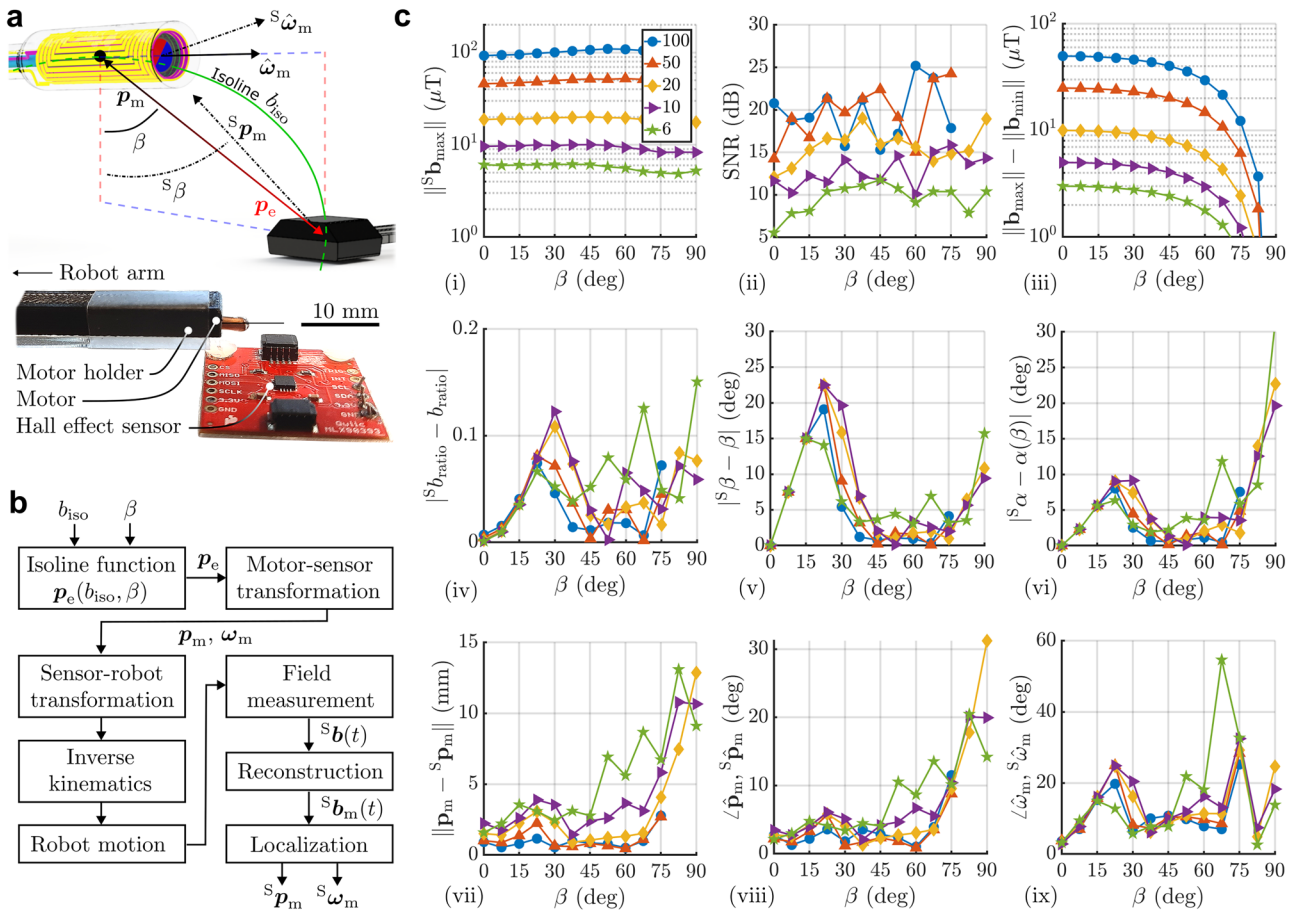

Fig. 6 | Magnetic localization of the permanent magnet synchronous motor (PMSM). a Experimental setup with a stationary Hall effect sensor and movable PMSM by a robotic arm. PMSM displacement moves the sensor along isoline positions ($\boldsymbol{p}_e(b_{iso}, \beta)$) of specific field strength (b_{iso}) and position angle (β). Real motor positions and rotation axis ($\boldsymbol{p}_m$, $\hat{\boldsymbol{\omega}}_m$) are known and compared to the measurement-based reconstructed motor pose. **b** Experimental procedure for magnetic localization. **c** Localization results for different isoline field strengths ($b_{iso} \in \{6, 10, 20, 50, 100\}$ μT) and position angles ($\beta \in [0, 90]$°), including (i) field strength, (ii) signal-to-noise ratio, (iii) theoretical difference in maximum and minimum field strengths, (iv) error between expected and reconstructed field ratio, (v) angular error in position angle, (vi) angular error in field angle, (vii) distance error in motor position, (viii) angular error in motor position vectors. (ix) Angular error in motor rotation axis.

mode, the electromagnet is off to prevent sensor saturation and interference with the motor. In manipulation mode, the PMSM is locked and behaves as a passive, radially magnetized permanent magnet. The electromagnet is on to generate a stationary field for PMSM steering, allowing mechanical rotation to change its deflection plane (Fig. 8d).

Quantitative results show successful entrance into all tube bifurcations, as well as forward and backward tracking over a total distance of 40 cm in 300 s (Fig. 8e and Supplementary Fig. 10). In localization mode, the PMSM operates at 1 Hz, and the sensor records data at 20 Hz over 2 s. Post-processing for pose reconstruction averaged 1 s, achieving a trajectory-following frequency of about 0.3 Hz.

Discussion

This study reports a magnetic localization method for in vivo rotatable dipoles, which herein is a new type of locking PMSM based on solid-liquid phase changing LMPA. The rotating field generated by the PMSM allows for the reconstruction of its position and rotation axis by and relative to a single magnetometer, with four possible solutions. Additionally, we integrated the magnetometer with an electromagnet to create an eye-in-hand sensorized mobile electromagnetic manipulation system. By demonstrating iterative PMSM localization and manipulation, we aimed to show the potential of closed mobile magnetic navigation systems to operate independently of fluoroscopic imaging.

PMSM design

The PMSM demonstrated that 2D fabricated flexible electronics may be used as 3D stators with combined functionality as sources of magnetic field and heat. Using the heat-generating property of stators has been used to achieve reversible rotor locking. The ferrofluid bearing minimized friction, opposed magnetic attraction between stators and rotor, and maintained concentricity during rotation (Supplementary Movie 1). However, manual fabrication (Fig. 2a) introduced functional inconsistencies. Alternatively, precise micro-fabricated parts should be considered for reliability and miniaturization[50]. Additionally, the application of excess ferrofluid encapsulated the rotor, preventing locking by the LMPA.

Rotor locking mechanism

The selection of Cerrolow 117 as the LMPA for reversible rotor locking was based on its 47 °C phase transition temperature, which is close to physiologically safe[27] and below NdFeB demagnetization temperatures[56]. Also, atomically similar LMPAs have a viscosity close to water[57] and a magnetic permeability close to air[58]. However, due to its liquid state and toxic elements, encapsulation is required for medical applications[53].

Temperature measurements of the PMSM show that internal LMPA phase transition can be reached at surface temperatures (≤44 °C) that prevent tissue injury (Fig. 3c)[27] Also, heating and cooling occur faster in water (37 °C) than in air (18 °C), with similar internal steady-state temperatures

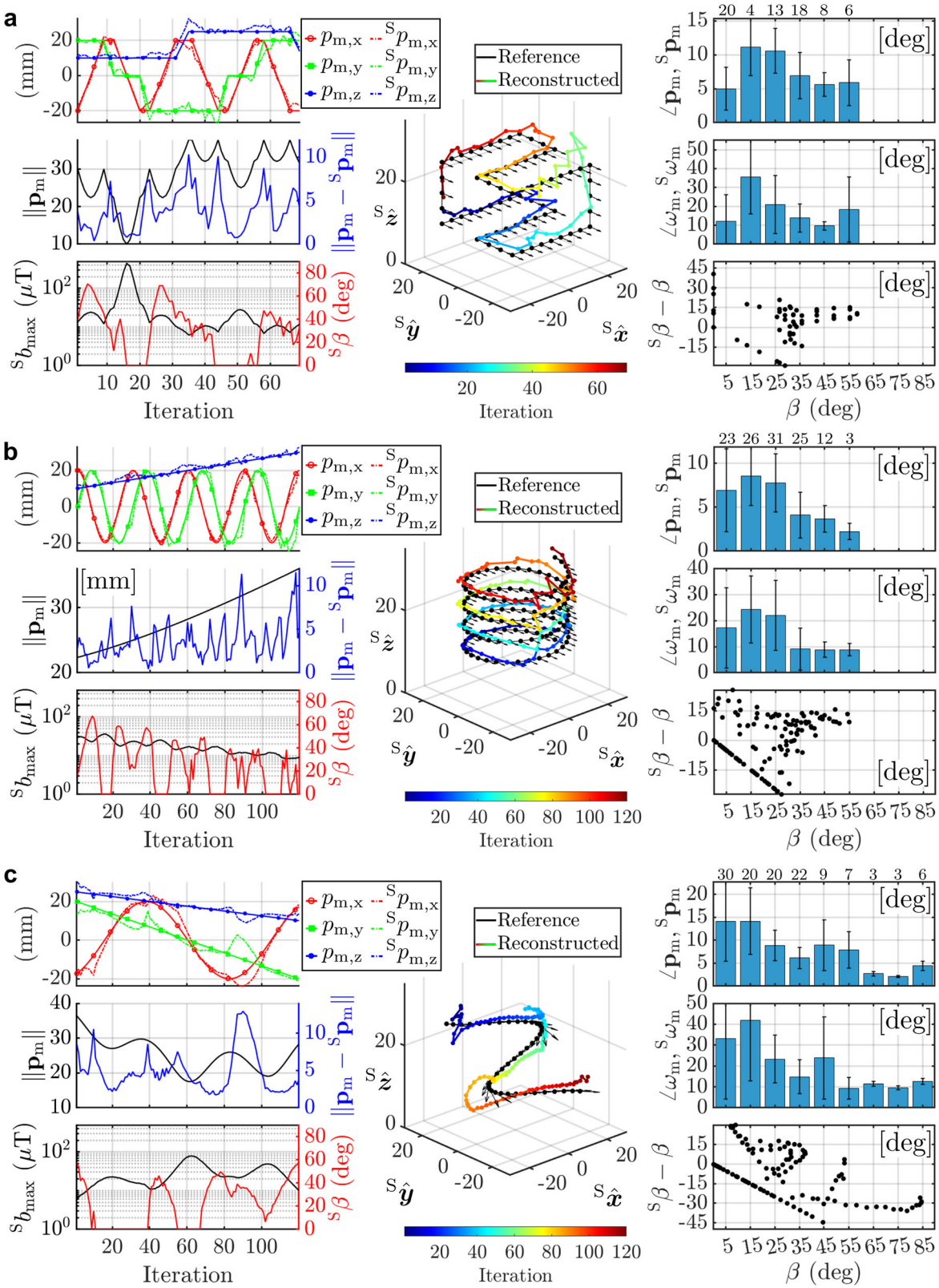

Fig. 7 | Tracking of the permanent magnet synchronous motor (PMSM) in 3D. Results show motor position ($\boldsymbol{p}_{\mathrm{m}}$, dots) and rotation axis ($\hat{\boldsymbol{\omega}}_{\mathrm{m}}$, arrows) with respect to the sensor frame, for **a** cubic, **b** spiral, and **c** sinusoidal paths. Error bars represent standard deviations with the associated number of samples annotated above each bar.

(49 °C). Surface temperature rises less in water (37–40 °C) than in air (18–31 °C). The system reaches steady-state in 20 s in water and 45 s in air, while passive cooling below the transition temperature takes just 2 s. This is indicative of the rate for switching between PMSM localization and manipulation modes. Therefore, mode-switching is limited by heating time.

Heating time during the rotor unlocking phase depends on power dissipation by the stators, which act as resistors. This process may be

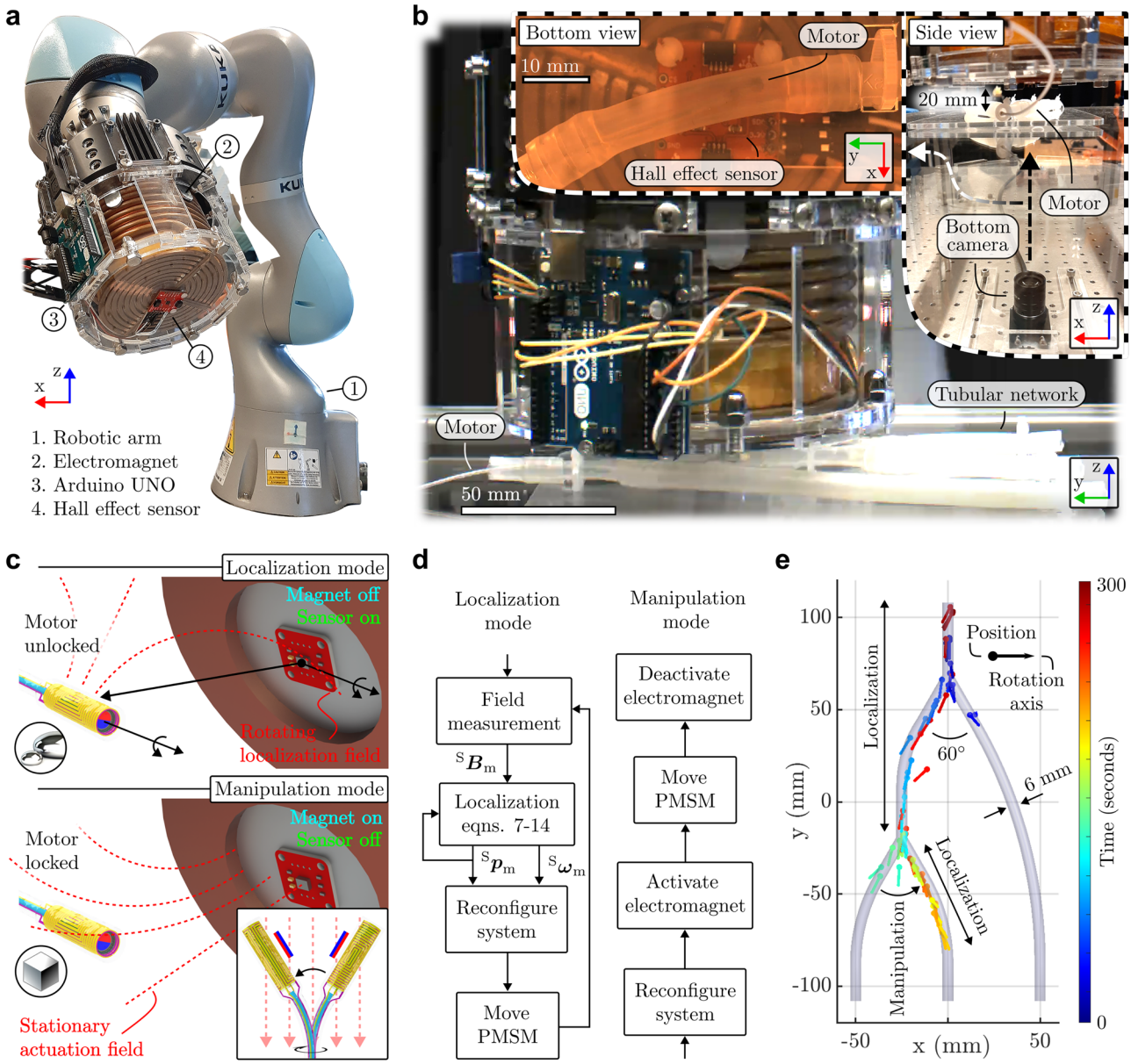

Fig. 8 | Magnetic localization and manipulation of the PMSM. a External system combining a robot arm, a Hall effect magnetometer, and an electromagnet. **b** Experimental setup including a tubular network enclosing the PMSM, vertically suspended electromagnet and magnetometer, and an upward-facing camera. **c** Different operating modes for localization and manipulation, alternating between PMSM (un)locked states, combined with external magnet or magnetometer (in)activity. **d** Flow diagram for the localization and manipulation modes. **e** Navigation results.

accelerated through a greater heat transfer rate, by increasing power dissipation with higher peak currents in the AC signal. However, for medical applications, temperature feedback would be required to maintain thermal biocompatibility[59].

Localization algorithm

The presented algorithm localizes a PMSM, modeled as a magnetic dipole with perpendicular rotation and magnetization axes. At its core, the algorithm uses precomputed rotor field isoline functions (Eqs. 4–6) that link rotating field properties to the rotating field source (Supplementary Fig. 7). By computing a ratio (b_{ratio}) of maximum and minimum field strengths ($\{b_{\max}, b_{\min}\}$) at a given position, the algorithm determines a set of isoline angles ($\{\beta, \alpha\}$) to rotate the measured field's rotation axis ($\hat{\boldsymbol{\omega}}_{\text{b}}$) into four possible combinations of dipole position and rotation axis ($\{\hat{\boldsymbol{p}}_{\text{m}}, \hat{\boldsymbol{\omega}}_{\text{m}}\}$) (Eqs. 8–10).

This fourfold ambiguity is also reported in previous work[32]. Herein, this is resolved using prior knowledge of dipole position. However, this method risks forwarding a previous faulty localization (Fig. 7). To prevent this, additional sensors may be mounted on the external manipulation system, enabling localization through triangulation.

Supporting the formulation of the isoline functions, we note that similar algorithms exist to localize a sensor based on the known temporal configuration of a rotating dipole[32,60,61]. However, in our reverse case, while similarly having access to field measurements, we have no information about the dipole rotation axis. This information is compensated for by formulating predetermined maps between rotating field components and the field source, i.e., the isoline functions.

Isoline function error sensitivity

The isoline functions exhibit different sensitivity to errors in field measurements depending on the relative configuration of the PMSM and sensor. Accordingly, regions of different localization error sensitivities may be distinguished around the rotor magnet[33,62].

The error sensitivity describes how errors in the measured field ratio (${}^{S}b_{\text{ratio}}$) affect errors in the isoline angles ($\{{}^{S}\beta, {}^{S}\alpha\}$). Partial derivatives indicate that $\partial\beta/\partial b_{\text{ratio}}$ is least sensitive for $b_{\text{ratio}} \in [1.1,\ 1.9]$, corresponding to $\beta \in [25,\ 75]°$ (Supplementary Fig. 8). Further, $|\partial\alpha/\partial\beta| \leq 1\ \forall\beta \in [0,\ 60]°$. This range corresponds to $b_{\text{ratio}} \in [1.4,\ 2]$, for which errors in ${}^{S}\beta$ are mitigated in ${}^{S}\alpha$ but amplified above. Therefore, PMSM directionality vectors $\{{}^{S}\hat{\boldsymbol{p}}_{\text{m}}, {}^{S}\hat{\boldsymbol{\omega}}_{\text{m}}\}$ are least sensitive to reconstruction errors in ${}^{S}b_{\text{ratio}}$ for relative rotor-sensor positions at $\beta \in [25,\ 60]°$, for which $b_{\text{ratio}} \in [1.4,\ 1.9]$. This region is supported by the localization experiments (Figs. 6 and 7).

Localization workspace

The localization workspace depends on the SNR of the rotor field measurement. The SNR is influenced by rotor size (magnetic moment) and sensor resolution, and noise. Here, the tri-axial Hall effect sensor has a 5 mT measurement range, ~3 μT peak noise (Supplementary Fig. 6), and 0.1 μT resolution. A minimum SNR of 10 dB was identified for localization (Fig. 6c). Accordingly, the workspace was limited to 40 mm distance from the sensor.

While this workspace is smaller than those using larger magnets[32,38] or more precise sensors[35,36], simulations suggest that reducing sensor noise could extend the workspace beyond 200 mm (Supplementary Fig. 11).

Localization accuracy

The localization accuracy, including angular errors in the PMSM's directionality vectors of position and rotation axis ($\{{}^{S}\hat{\boldsymbol{p}}_{\text{m}}, {}^{S}\hat{\boldsymbol{\omega}}_{\text{m}}\}$), depends on angular errors in the (direction of) measured minimum field strength and rotation axis ($\{{}^{S}\boldsymbol{b}_{\text{min}}, {}^{S}\hat{\boldsymbol{\omega}}_{\text{b}}\}$), as well as errors in the isoline angles ($\{{}^{S}\beta, {}^{S}\alpha\}$) (Eqs. 11–13). These are influenced by the sensor's SNR, accuracy, and precision. In this work, angular errors of 5–10° in ${}^{S}\hat{\boldsymbol{p}}_{\text{m}}$ and 10–30° error in ${}^{S}\hat{\boldsymbol{\omega}}_{\text{m}}$ were observed for a cylindrical rotor magnet (1 mm diameter, 3 mm length) along various 3D trajectories (Fig. 7).

Alternative sources of error, such as micrometer-range eccentricity during rotor rotation (Supplementary Movie 1) is considered negligible due to its near-zero field gradient (Fig. 3f). The stator field is similarly considered negligible, as its strength is one to two orders weaker than the rotor field (Supplementary Fig. 6). To improve localization accuracy, we hypothesize including localization methods for stationary magnets[31], as the rotor magnet's field (after filtering Earth's field) could be treated as stationary at each instant.

Localization frequency

The localization frequency (0.3 Hz) depends on the rate of rotor rotation (1 Hz), sensor sampling frequency (20 Hz), the number of samples (40), and computation time. Higher localization frequencies can be achieved using faster sampling or reducing the number of samples (speeding up measurement time and data processing). In combination, the rotor rotation rate could be increased, which was shown up to 10 Hz (Fig. 3i and Supplementary Movie 1). Faster rotor rotation rates may be achieved by increasing the current through the stators, at a cost of temperature elevation.

Magnetic manipulation

Magnetic manipulation was performed iteratively with localization, rather than simultaneously[30,60]. This was necessary due to saturation of the eye-in-hand Hall effect sensor upon activation of the electromagnet. Additionally, the manipulation field, typically up to a few tens of milli-Tesla[9], is an order of magnitude stronger than the stator fields (Fig. 3b and Supplementary Fig. 6), which interfere with rotor rotation.

Rudimentary PMSM localization-informed system reconfiguration and manipulation were shown, limited to electromagnet displacement along the reconstructed motor rotation axis (Fig. 8c and Supplementary Movie 4). More advanced manipulation could be achieved by incorporating an electromagnet field model for model- and localization-informed reconfiguration[16].

Finally, due to the unknown radial orientation of the PMSM magnetic moment, initial application of a manipulation field causes deflection in an indeterminate plane. As a solution, we hypothesize that for synchronous motors, frequency analysis and sinusoidal fitting of field measurements can provide a time-dependent function to predict the direction of magnetic moment and, therefore, plane of deflection.

Future work

The efficacy of PMSM localization can be increased by improving sensor noise, resolution, and count. Integrating the presented algorithm with those for stationary magnets may further improve accuracy. For dipoles rotating at a constant frequency, sinusoidal fitting could be used to estimate rotor orientation and predict PMSM deflection. Multiple PMSMs with distinct frequencies could be simultaneously located via frequency analysis. The localization method may be applied to any structure incorporating or representing a rotating magnetic dipole with perpendicular magnetization and rotation axes, such as intravascular imaging catheters[50], swimming robots[63], mechanically rotated continuum robots[7], and magnetically actuated untethered robots[64]. Beyond localization, local PMSM-generated rotating fields could be used in vivo, such as for actuation of microrobots[65,66], wireless power transfer to implants[67], or aid in nerve regeneration[68] and cancer therapy[69,70].

Materials and methods

Fabrication of planar coils

Planar coils were fabricated from a 55 μm thick polyimide copper clad laminate (IM30-LM-000122, Goodfellow GmbH, Germany), comprising 25 μm thick polyimide, 12 μm epoxy adhesive, and 18 μm copper. The coils were prepared using optical lithography and wet etching processes. First, the copper surface was cleaned using O_2 plasma for 2 min. Then, the AZ5214 photoresist (MicroChemicals GmbH, Germany) was spin-coated at 3000 rpm for 30 s and baked at 100 °C for 2 min. The coil structure was patterned using a direct UV-laser writer (DWL66, Heidelberg Instruments, Germany) with a 410 nm wavelength. The desired structure was revealed in 1:4 solution of AZ351b developer in deionized water. The laminate was subjected to post-baking at 100 °C for 2 min to ensure better adhesion of photoresist during wet etching. Thereafter, the laminate was wet etched at 60 °C in 1:10 sodium persulfate solution in DI water (B327, AG TermoPasty, Grzegorz Gasowski, Poland). Residual etching agent was removed with DI water, and the photoresist was cleaned off with acetone, isopropanol, and DI water.

Two versions of the planar coil were made (inner and outer) (Supplementary Fig. 1a). Each coil has 12 windings. (1) The inner coil has a length of 5.5 mm and a width of 4.35 mm. Copper strands have a width of 0.13 mm. Longitudinal strands are spaced 0.05 mm. Transverse strands are spaced 0.07 mm. The coil has a resistance of 0.9 Ω. (2) The outer coil has a length of 5.5 mm and a width of 4.8 mm. Copper strands have a width of 0.15 mm. Longitudinal strands are spaced 0.05 mm. Transverse strands are spaced 0.05 mm. The coil has a resistance of 0.82 Ω.

Assembly of the PMSM

Enameled copper leads with a 50 μm diameter (TRU Components, Conrad Electronic SE) are soldered to the terminals of the planar coils (Supplementary Fig. 1b). The coils are aligned and adhered with a 1.2 mm transverse offset using 50 μm thick double-sided tape (tesa® 61250) placed around the leads (Fig. 2a(i)), then inserted into a PVDF heat shrinkable tube (hellermanntyton 311-00169, Farnell) of 1.6 mm inner diameter, 1.9 mm outer diameter, and 7 mm length ((Fig. 2a(ii))). The coils' center-to-center offset displacement provides perpendicular angular orientation between the wrapped coils.

The copper leads are threaded through a PTFE tube with a 0.66 mm inner and 0.96 mm outer diameter (ptfetubeshop, The Netherlands) (Fig. 2a(ii)), that serves as a protective tether and additionally houses a polyetheretherketone (PEEK) mandrel with 0.38 mm diameter (Zeus Industral Inc., USA). Heat is applied at 200 °C to shrink the PVDF tube, connecting it to the PTFE tether (Fig. 2a(iii)). Thereafter, low-friction resin (durable resin, Formlabs) is injected into the stator lumen, pushed down

using a steel rod of 1.2 mm diameter, and UV-cured at 60 °C for 60 min (Form Cure, Formlabs), creating an airtight seal for the lumen and rigid connection to the PEEK mandrel.

A solid cylinder of fusible alloy (Cerrolow 117, Bolton Metal Products Co., Inc., USA) is placed in the rotor lumen (Fig. 2a(iv)). This cylinder is made by injecting liquefied alloy into a silicone tube of 1 mm inner diameter, followed by cooling and solidification, cutting to a 3 mm length with a Stanley knife, and subsequent removal of the cylinder from the tube. Then, a constant current of 150 mA is applied to the inner stator, resulting in heating and liquefying the alloy. Thereafter, a diametrically magnetized rotor of 1 mm diameter and 3 mm length (SP0103DM-50, First4Magnets, UK), partially coated with ferrofluidic bearing (M-FER-10, Supermagnete, The Netherlands), is inserted and submerged in the liquefied alloy (Fig. 2a(v)). Consequently, the alloy fills the space around the rotor and is pushed upwards toward the distal exit of the stator lumen (Fig. 2a(vi)). Upon deactivation of the stator, the alloy solidifies. Finally, the assembled motor is dip-coated in UV-curable resin (durable resin, Formlabs) and cured at 40 °C to prevent intermediate phase transition of the alloy during curing, as well as leakage during activation (Fig. 2a(vii)).

PMSM thermal characterization

Thermal characterization was performed in air (18 °C) and distilled water (37 °C), with the permament magnet synchronous motor (PMSM) having an empty rotor cavity, i.e., without an internal rotor magnet or fusible alloy (see Fig. 2b). Quadrature currents were applied to the inner ($I_{\text{inner}} = I\cos(2\pi f_{\text{m}} t)$) and outer stator ($I_{\text{outer}} = I\sin(2\pi f_{\text{m}} t)$), with constant amplitude ($I = 200$ mA) and unit frequency ($f_{\text{m}} = 1$ Hz).

Temperature measurements were obtained using a 1 mm diameter K-type thermocouple connected to a thermocouple-to-digital converter module (Diligent Pmod TC1, RS PRO, 134-6476) and an Arduino Nano during resistive heating ($t \in [0, 120]$ s) and passive cooling ($t \in [120, 180]$). The thermocouple was positioned both on the outer surface of the PMSM and inside the rotor cavity to measure external and internal temperature increase, respectively (Supplementary Fig. 3).

Rotor field model

We present an analytical model for accurately describing the magnetic field generated by cylindrical radially magnetized permanent rotors. The rotor volume is discretized into subvolumes, each modeled as a field source using a multipole expansion model. Symmetry of the multipole expansion models among these subvolume field sources ensures axisymmetry of the magnetic field around the rotor's magnetization axis. This model is herein referred to as an FE-inspired multipole/source expansion model.

Let ${}^{\text{R}}\boldsymbol{R} = [{}^{\text{R}}\hat{\boldsymbol{x}}, {}^{\text{R}}\hat{\boldsymbol{y}}, {}^{\text{R}}\hat{\boldsymbol{z}}] \in \text{SO}(3)$ be the rotor's local reference frame at its center of mass. Here, ${}^{\text{R}}\hat{\boldsymbol{z}}$ is the longitudinal axis, $\{{}^{\text{R}}\hat{\boldsymbol{x}}, {}^{\text{R}}\hat{\boldsymbol{y}}\}$ the radial axes, and ${}^{\text{R}}\boldsymbol{\mu} = {}^{\text{R}}\hat{\boldsymbol{x}}$ the magnetization axis. We also define a position vector ($\boldsymbol{p} := {}^{\text{R}}\boldsymbol{p} = \langle {}^{\text{R}}x, {}^{\text{R}}y, {}^{\text{R}}z\rangle$) expressed in ${}^{\text{R}}\boldsymbol{R}$.

Given a base harmonic scalar potential (${}^{\text{R}}\Psi_0(\boldsymbol{p} = 1/\|\boldsymbol{p}\|)$) that satisfies Laplace's equation, the corresponding field function (${}^{\text{R}}\boldsymbol{b}_0(\boldsymbol{p}) = \partial({}^{\text{R}}\Psi_0)/\partial\boldsymbol{p}$) is divergence- and curl-free as required by Maxwell's equations in current-free space. This property extends to higher-order derivatives of the scalar potential with respect to the magnetization axis (${}^{\text{R}}\Psi_u(\boldsymbol{p}) = \partial^u({}^{\text{R}}\Psi_0)/\partial x^u$, $u \in \mathbb{N}$), and their associated fields (${}^{\text{R}}\boldsymbol{b}_u(\boldsymbol{p}) = \partial({}^{\text{R}}\Psi_u(\boldsymbol{p}))/\partial\boldsymbol{p}$), as well as those scaled by scalar coefficients ($a_u \in \mathbb{R}$). Scalar potentials with $u \in 2\mathbb{N}$ provide field functions ${}^{\text{R}}\boldsymbol{b}_u(\boldsymbol{p})$ that contain (unpaired) monopole terms, such as tripole ($u = 2$) or pentapole ($u = 4$). The natural absence of monopoles therefore constrains $u \in 2\mathbb{N} + 1$ to be uneven.

Scalar potentials are assigned to subvolumes of the rotor, with displacement vectors ($\Delta\boldsymbol{p}_v$, $v \in \mathbb{N}$) relative to ${}^{\text{R}}\boldsymbol{R}$. These vectors are part of a symmetric set ($\Delta\mathbb{P}_v$) with respect to the planes spanned by the principal axes in ${}^{\text{R}}\boldsymbol{R}$:

$$\Delta\mathbb{P}_v = \{\Delta\boldsymbol{p}_v^{+++}, \Delta\boldsymbol{p}_v^{++-}, \Delta\boldsymbol{p}_v^{+-+}, \Delta\boldsymbol{p}_v^{-++}, \Delta\boldsymbol{p}_v^{+--}, \Delta\boldsymbol{p}_v^{-+-}, \Delta\boldsymbol{p}_v^{--+}, \Delta\boldsymbol{p}_v^{---}\},$$

where $\Delta\boldsymbol{p}_v^{\pm\pm\pm}$ has positive/negative xyz-components, and $\Delta\mathbb{P}_{v,i}$ is the ith $\in \{1, 2, \ldots, 8\}$ displacement vector. Symmetry of the field model around the magnetization axis requires coefficients for pole-specific scalar potentials to be equal for all displacement vectors in a symmetric set. Accordingly, the base harmonic scalar potential is formulated:

$${}^{\text{R}}\Psi_{0,v}(\boldsymbol{p}) = \sum_{i=1}^{8} \frac{1}{\|\,\boldsymbol{p} - \Delta\mathbb{P}_{v,i}\,\|}, \tag{1}$$

leading to the field expression for a symmetric set of source displacement vectors:

$$\begin{aligned} {}^{\text{R}}\boldsymbol{b}_v(\boldsymbol{p}) &= \sum_{u=0} a_{2u+1,v} \cdot \frac{\partial}{\partial\boldsymbol{p}} \left(\frac{\partial^{2u+1}}{\partial x^{2u+1}} \left({}^{\text{R}}\Psi_{0,v} \right) \right) \\ &= a_{1,v}\, {}^{\text{R}}\boldsymbol{b}_{1,v} + a_{3,v}\, {}^{\text{R}}\boldsymbol{b}_{3,v} + a_{5,v}\, {}^{\text{R}}\boldsymbol{b}_{5,v} + \ldots, \\ &= \underbrace{\left[{}^{\text{R}}\boldsymbol{b}_{1,v}\ {}^{\text{R}}\boldsymbol{b}_{3,v} \ldots \right]}_{{}^{\text{R}}\boldsymbol{B}_v(\boldsymbol{p})} \underbrace{\left[a_{1,v} a_{3,v} \ldots \right]^T}_{\boldsymbol{a}_v}. \end{aligned} \tag{2}$$

Finally, the FE-inspired multipole/source expansion model is given by:

$${}^{\text{R}}\boldsymbol{b}(\boldsymbol{p}) = \sum_{v=1} {}^{\text{R}}\boldsymbol{B}_v(\boldsymbol{p})\boldsymbol{a}_v = \underbrace{\left[{}^{\text{R}}\boldsymbol{B}_1\ {}^{\text{R}}\boldsymbol{B}_2 \ldots \right]}_{{}^{\text{R}}\boldsymbol{B}(\boldsymbol{p})} \underbrace{\left[\boldsymbol{a}_1^T\ \boldsymbol{a}_2^T \ldots \right]^T}_{\boldsymbol{a}}. \tag{3}$$

This model was implemented using MATLAB's symbolic toolbox (MATLAB R2024, The Mathworks, Natick, Massachusetts, USA). The model coefficients were obtained by linear least squares regression with field estimates ${}^{\text{R}}\tilde{\boldsymbol{b}}(\boldsymbol{p})$ obtained from a measurement-based scaled FEM of the rotor (COMSOL, Burlington, VT, USA), according to $\boldsymbol{a} = ({}^{\text{R}}\boldsymbol{B}(\boldsymbol{p})^{\dagger})\, {}^{\text{R}}\tilde{\boldsymbol{b}}(\boldsymbol{p})$, where $*^{\dagger}$ represents the pseudoinverse.

Rotor field isoline functions

Within the formulation of the following rotor field isoline functions, we again consider ${}^{\text{R}}\boldsymbol{R} = [{}^{\text{R}}\hat{\boldsymbol{x}}, {}^{\text{R}}\hat{\boldsymbol{y}}, {}^{\text{R}}\hat{\boldsymbol{z}}] \in \text{SO}(3)$ as the rotor's local reference frame in its center of mass, ${}^{\text{R}}\hat{\boldsymbol{x}}$ and ${}^{\text{R}}\hat{\boldsymbol{z}}$ to span the rotor's magnetization plane, $\hat{\boldsymbol{\mu}} := {}^{\text{R}}\hat{\boldsymbol{x}}$ as the rotor's magnetization axis, and $\hat{\boldsymbol{\omega}}_{\text{m}} := {}^{\text{R}}\hat{\boldsymbol{z}}$ as the rotor's rotation axis.

Isoline position. The isoline position vector function ($\boldsymbol{p}_{\text{e}}(b_{\text{iso}}, \beta) : \mathbb{R}^2 \to \mathbb{R}^2$) traces the circumference of two-dimensional, ellipse-shaped field isolines of uniform strength (b_{iso}) as a function of a position angle (β) relative to the rotor's magnetization axis (see Fig. 4). This function is formulated as:

$$\boldsymbol{p}_{\text{e}}(b_{\text{iso}}, \beta) = \langle c_{\text{x}}(b_{\text{iso}})\cos(\beta),\ c_{\text{z}}(b_{\text{iso}})\sin(\beta)\rangle, \tag{4}$$

with $c_{\text{x}}(b_{\text{iso}})$ and $c_{\text{z}}(b_{\text{iso}})$ coefficients dependent on the isoline field strength, modeled as second-order power functions: $c_{\text{x}}(b_{\text{iso}}) = c_{\text{x},1} b_{\text{iso}}^{c_{\text{x},2}} + c_{\text{x},3}$, with $c_{\text{x},i} (i \in \{1, 2, 3\})$ the power function parameters. The same model applies to $c_{\text{z}}(b_{\text{iso}})$.

To calculate the power function parameters, the rotor field function ${}^{\text{R}}\boldsymbol{b}(\boldsymbol{p})$ is used to compute the magnetic field strength at various positions on a 2D grid within the magnetization plane. MATLAB's *contour* function then generates matrices of 2D position vectors corresponding to different elliptical contour levels (b_{iso}). The ellipse coefficients ($c_{\text{x}}(b_{\text{iso}})$, $c_{\text{z}}(b_{\text{iso}})$) for each contour level are then obtained using the *fit_ellipse* function[71]. Finally, the independent parameters of the power functions ($c_{\text{x},i}$, $c_{\text{z},i}$) are determined using MATLAB's *curve fitting* toolbox.

Isoline field ratio. The isoline field ratio scalar function ($b_{\text{ratio}}(\beta) : \mathbb{R} \to \mathbb{R}$) describes the ratio of maximum to minimum magnetic field strength

at isoline position angles (β). This function is formulated as:

$$b_{\text{ratio}}(\beta) = a_0 + \sum_{k=1}^{8}\left(a_k \cos(k\beta w) + b_k \sin(k\beta w)\right), \tag{5}$$

where a_k, b_k, and w are Fourier coefficients.

To determine these coefficients, we select an isoline field strength ($b_{\text{iso}} = 100\ \mu\text{T}$) and compute the field ratio over a range of position angles ($\beta \in \{1, 2, \ldots, 360\}°$). The corresponding 2D isoline positions ($\boldsymbol{p}_e(b_{\text{iso}}, \beta) = \langle p_{e,x}, p_{e,z}\rangle$) are computed, and a 3D variant is defined as $\tilde{\boldsymbol{p}}_e(b_{\text{iso}}, \beta) = \langle p_{e,x}, 0, p_{e,z}\rangle$.

Using the 3D rotor field function (${}^{R}\boldsymbol{b}(\boldsymbol{p})$), maximum field ($b_{\max}(\beta) = \| {}^{R}\boldsymbol{b}(\tilde{\boldsymbol{p}}_e(b_{\text{iso}}, \beta)) \|$) and minimum field strength ($b_{\min}(\beta) = \| \boldsymbol{R}_z(\pi/2)\, {}^{R}\boldsymbol{b}(\boldsymbol{R}_z(\pi/2)^{T}\tilde{\boldsymbol{p}}_e(b_{\text{iso}}, \beta)) \|$) are calculated for each angle β, where $\boldsymbol{R}_z \in \text{SO}(3)$ is a rotation matrix corresponding to the rotor's rotation axis ($\hat{\boldsymbol{\omega}}_m := {}^{R}\hat{\boldsymbol{z}}$). The field ratio is then determined as $b_{\text{ratio}}(\beta) = b_{\max}(\beta)/b_{\min}(\beta)$. Finally, the Fourier coefficients are obtained using MATLAB's *curve fitting* toolbox, applying an 8-term Fourier series to fit $b_{\text{ratio}}(\beta)$ across the range of β.

Isoline field angle. The isoline field angle scalar function ($\alpha(\beta) : \mathbb{R} \to \mathbb{R}$) decribes the angle between the isoline position vector and the field rotation axis. This function is formulated as:

$$\alpha(\beta) = a_0 + \sum_{k=1}^{20} a_k \cos(2\pi f_k \beta - b_k), \tag{6}$$

where a_k, f_k, and b_k are Fourier parameters.

To determine these parameters, we again select an isoline field strength ($b_{\text{iso}} = 100\ \mu\text{T}$) and range of position angles ($\beta \in \{1, 2, \ldots, 360\}°$), and compute 2D isoline positions ($\boldsymbol{p}_e(b_{\text{iso}}, \beta) = \langle p_{e,x}, p_{e,z}\rangle$), a 3D variant $\tilde{\boldsymbol{p}}_e(b_{\text{iso}}, \beta) = \langle p_{e,x}, 0, p_{e,z}\rangle$, and maximum field strength ($\boldsymbol{b}_{\max}(\beta) = {}^{R}\boldsymbol{b}(\tilde{\boldsymbol{p}}_e(b_{\text{iso}}, \beta))$) and minimum field strength ($\boldsymbol{b}_{\min}(\beta) = \boldsymbol{R}_z(\pi/2)\, {}^{R}\boldsymbol{b}(\boldsymbol{R}_z(\pi/2)^{T}\tilde{\boldsymbol{p}}_e(b_{\text{iso}}, \beta))$). The field rotation axis at each β is then computed as $\hat{\boldsymbol{\omega}}_b(\beta) = \hat{\boldsymbol{b}}_{\max}(\beta) \times \hat{\boldsymbol{b}}_{\min}(\beta)$, where $\hat{*}$ denotes a unit vector. The isoline field angle is then obtained as $\alpha(\beta) = \cos^{-1}(\hat{\tilde{\boldsymbol{p}}}_e \cdot \boldsymbol{\omega}_b(\beta))$. Finally, the Fourier parameters, including amplitudes (a_k), frequencies (f_k), and phases (b_k), are obtained with the *ft_spect* function[72].

Motor field properties

A PMSM driven by quadrature currents in the inner ($I_{\text{inner}} = I\sin(2\pi f_m t)$) and outer ($I_{\text{outer}} = I\cos(2\pi f_m t)$) stators at a given motor frequency (f_m) generates a rotating magnetic field (${}^{S}\boldsymbol{b}_m(t)$). Field measurements are taken with a Hall effect sensor (MLX90371, Melexis, Ypres, Belgium) positioned around the PMSM, at a sampling frequency, $f_s = 20$ Hz. The sensor samples the tri-axial magnetic field (${}^{S}\boldsymbol{b}(t) = {}^{S}\boldsymbol{b}_0 + {}^{S}\boldsymbol{b}_m(t) + \boldsymbol{n}_s(t)$), which includes Earth's static field (${}^{S}\boldsymbol{b}_0$), the motor field ${}^{S}\boldsymbol{b}_m(t)$, and sensor noise ($\boldsymbol{n}_s(t)$).

Tri-axial field measurements recorded at discrete time instants ($i\Delta t$), where $\Delta t = 1/f_s$, are stored in matrix form (${}^{S}\boldsymbol{B} = [{}^{S}\boldsymbol{b}(t_0), {}^{S}\boldsymbol{b}(t_1), \ldots, {}^{S}\boldsymbol{b}(t_M)]$). Fourier-derived frequency-specific amplitudes ($\boldsymbol{A}_{\text{fft}}(f)$) are obtained with MATLAB's *fft* function, giving the Earth's field as ${}^{S}\boldsymbol{b}_0 = \boldsymbol{A}_{\text{fft}}(0)$. The motor field measurements matrix (${}^{S}\boldsymbol{B}_m = [{}^{S}\boldsymbol{b}_m(t_0), {}^{S}\boldsymbol{b}_m(t_1), \ldots, {}^{S}\boldsymbol{b}_m(t_M)]$) is then computed, with ${}^{S}\boldsymbol{b}_m(t_i) = {}^{S}\boldsymbol{b}(t_i) - {}^{S}\boldsymbol{b}_0$.

Considering zero noise, ${}^{S}\boldsymbol{b}_m(t)$ forms an ellipse and rotates in a plane with a normal vector equal to the field's rotation axis (${}^{S}\hat{\boldsymbol{\omega}}_b$), computed using the following minimization problem implemented with MATLAB's *fmincon*:

$$\pm\, {}^{S}\hat{\boldsymbol{\omega}}_b = \arg\min_{\hat{\boldsymbol{\omega}}} \sum_{i=0}^{M} \sqrt{\left(\hat{\boldsymbol{\omega}} \cdot {}^{S}\hat{\boldsymbol{b}}_m(t_i)\right)^2}, \tag{7}$$

where $\hat{*}$ denotes a unit vector. Further, we fit a 3D ellipse to ${}^{S}\boldsymbol{B}_m$, whose principal axes correspond to the vectors of maximum and minimum field strength. To this end, we define a rotation matrix (${}^{S}_{E}\boldsymbol{R} = [{}^{S}\hat{\boldsymbol{x}}_E, {}^{S}\hat{\boldsymbol{y}}_E, {}^{S}\hat{\boldsymbol{z}}_E]$) between the sensor and field ellipse frame where ${}^{S}\hat{\boldsymbol{z}}_E = {}^{S}\hat{\boldsymbol{\omega}}_b$, and ${}^{S}\hat{\boldsymbol{x}}_E \times {}^{S}\hat{\boldsymbol{y}}_E = {}^{S}\hat{\boldsymbol{z}}_E$ is arbitrary. The motor field measurements are projected onto the 2D ellipse plane as ${}^{E}\boldsymbol{B}_m = \left({}^{S}_{E}\boldsymbol{R}^{T}\right) {}^{S}\boldsymbol{B}_m$. A 2D ellipse is then fit to the *xy*-components (${}^{E}\boldsymbol{B}_{m,xy}$) using the *fit_ellipse* function implemented in MATLAB[71]. Given sufficient data points, it is assumed that sensor noise ($\boldsymbol{n}_s(t)$) is averaged out during the fitting of the ellipse. The principal axes of this ellipse represent the vectors of maximum (${}^{E}\boldsymbol{b}_{\max,xy}$) and minimum (${}^{E}\boldsymbol{b}_{\min,xy}$) field strength. Their respective 3D representations (${}^{E}\boldsymbol{b} = \langle {}^{E}\boldsymbol{b}_{xy}, 0\rangle$) are then transformed back to the sensor's reference frame, yielding ${}^{S}\boldsymbol{b}_{\max} = \left({}^{S}_{E}\boldsymbol{R}\right) {}^{E}\boldsymbol{b}_{\max}$ and ${}^{S}\boldsymbol{b}_{\min} = \left({}^{S}_{E}\boldsymbol{R}\right) {}^{E}\boldsymbol{b}_{\min}$. Finally, the field ratio is obtained as ${}^{S}b_{\text{ratio}} = \| {}^{S}\boldsymbol{b}_{\max} \| \,/\, \| {}^{S}\boldsymbol{b}_{\min} \|$. Given the theoretical limits of field ratio ($b_{\text{ratio}}(\beta) \in [1, 2]$), any measured ${}^{S}b_{\text{ratio}}$ that falls outside this range is adjusted to the nearest boundary value.

Reconstruction of motor pose

The motor pose relative to and expressed in the sensor frame {*S*} is defined by the motor's position (${}^{S}\boldsymbol{p}_m$) and rotation axis (${}^{S}\boldsymbol{\omega}_m$). These vectors are computed using the measured motor field properties ($\{{}^{S}\hat{\boldsymbol{\omega}}_b, {}^{S}\boldsymbol{b}_{\max}, {}^{S}\boldsymbol{b}_{\min}, {}^{S}b_{\text{ratio}}\}$) and rotor field isoline functions, including isoline position ($\boldsymbol{p}_e(b_{\text{iso}}, \beta)$), field ratio ($b_{\text{ratio}}(\beta)$), and field angle ($\alpha(\beta)$).

An isoline position in the rotor's magnetization plane is matched to the sensor's motor field measurements according to:

$${}^{S}\beta = \arg\min_{\beta \in [0, \pi/2]} |\, {}^{S}b_{\text{ratio}} - b_{\text{ratio}}(\beta)|, \tag{8}$$

$${}^{S}\boldsymbol{p}_e = \boldsymbol{p}_e({}^{S}b_{\text{iso}}, {}^{S}\beta), \tag{9}$$

$${}^{S}\alpha = \alpha({}^{S}\beta), \tag{10}$$

where ${}^{S}b_{\text{iso}} = \| {}^{S}\boldsymbol{b}_{\max} \|$ is the measured isoline field strength. Because the vectors ${}^{S}\boldsymbol{b}_{\max}$ and ${}^{S}\hat{\boldsymbol{\omega}}_b$ span the reconstructed magnetization plane, with ${}^{S}\boldsymbol{b}_{\min}$ being perpendicular to this plane, a rotation matrix $\boldsymbol{R}_{\min}(\psi) \in \text{SO}(3)$ is defined based on the rotation vector ${}^{S}\hat{\boldsymbol{b}}_{\min}\psi$, and the motor pose is computed as:

$${}^{S}\hat{\boldsymbol{p}}_m = c_1 \boldsymbol{R}_{\min}(c_2\, {}^{S}\alpha)\, {}^{S}\hat{\boldsymbol{\omega}}_b, \tag{11}$$

$${}^{S}\boldsymbol{p}_m = {}^{S}\hat{\boldsymbol{p}}_m \cdot \| {}^{S}\boldsymbol{p}_e \|, \tag{12}$$

$${}^{S}\hat{\boldsymbol{\omega}}_m = c_2 \boldsymbol{R}_{\min}\left(c_2 \cdot ({}^{S}\alpha - {}^{S}\beta + c_2\pi/2)\right) {}^{S}\hat{\boldsymbol{\omega}}_b, \tag{13}$$

where $c_j \in \{-1, 1\} (j \in \{1, 2\})$ are coefficients that represent rotation direction. Herein, the coefficients are determined based on a previously known or reconstructed motor position vector (${}^{S}\hat{\boldsymbol{p}}_m(t_{i-1})$) according to:

$$\{c_1, c_2\} = \arg\min_{c_1, c_2 \in \{-1,1\}} \cos^{-1}\left({}^{S}\hat{\boldsymbol{p}}_m(t_{i-1}) \cdot {}^{S}\hat{\boldsymbol{p}}_m(t_i)\right). \tag{14}$$

In the herein presented demonstrations of magnetic localization and manipulation, the initial motor position vector (${}^{S}\hat{\boldsymbol{p}}_m(t_0)$) was provided to the localization algorithm.

Magnetic localization and manipulation

The magnetic localization and manipulation hardware includes an external integrated Hall effect sensor (MLX90371, Melexis, Belgium), a custom electromagnetic coil, and a robotic arm (Kuka LBR IIwa-14 R821, Augsburg, Germany), as well as an internal PMSM. The PMSM navigates a custom tubular network of opaque silicone tubes and Y-shaped connectors, each

with a 6 mm inner diameter, demonstrating 2D localization and manipulation thereof in the horizontal *xy*-plane.

For localization, the external system provides the sensor's temporal orientation $({}^{S}_{E}\boldsymbol{R}$ and position $({}^{B}\boldsymbol{p}_{S}$ relative to base of the robot. When the PMSM is active and near the sensor, the pose reconstruction using the measured motor field matrix $({}^{S}\boldsymbol{B}_{m})$ leads to the motor position $({}^{S}\boldsymbol{p}_{m})$ and rotation axis $({}^{S}\hat{\boldsymbol{\omega}}_{m})$ relative to both the sensor and robot base, calculated as ${}^{B}\boldsymbol{p}_{m} = {}^{B}\boldsymbol{p}_{S} + {}^{S}_{B}\boldsymbol{R}\,{}^{S}\boldsymbol{p}_{m}$ and ${}^{B}\hat{\boldsymbol{\omega}}_{m} = {}^{S}_{B}\boldsymbol{R}\,{}^{S}\hat{\boldsymbol{\omega}}_{m}$. The robot then repositions the sensor horizontally above the calculated motor position.

For manipulation, when the PMSM is inactive, the electromagnet is displaced 20 mm along the *xy*-projection of the last reconstructed ${}^{B}\hat{\boldsymbol{\omega}}_{m}$. The electromagnet generates a static magnetic field across the PMSM, which is manually rotated to alter its magnetization direction and deflection plane. The electromagnet is then turned off and reset to its initial position.

Motor power system

The motor power system comprises a custom-designed coil driver connected to the stator leads of the PMSM (Supplementary Fig. 12). The coil driver includes a bidirectional DC triple motor controller shield (Motoron M3S256, Pololu Robotics) connected to an Arduino UNO. Each output of the shield is connected in series to a custom inductor (~50 μH), made of a 6 mm diameter ferrite core (RSPro, Fair-Rite, 172-9993) and manually wound 0.5 mm diameter copper wire, and a current sensor (ACS712 5A, AZDelivery).

The output signal of the current sensor is smoothened by a 10 nF ceramic capacitor placed between its ground and output pins. This current sensor is used in closed-loop current regulation, managed by a custom-designed PID controller. The Arduino board is powered via a PC with a serial communication to command the current amplitudes and frequencies for stator activation. Finally, the motor shield is powered through a socket connected to a 240 V AC to 24 V DC transformer, which is then stepped down to 8 V using a DC-DC converter (LM2596S, AZDelivery).

Data availability

The authors declare that data supporting the findings of this study are available within the paper and its Supplementary Information files.

Code availability

All the relevant code used to generate the results in this paper and supplementary information are available from the corresponding author upon reasonable request.

Received: 14 November 2024; Accepted: 29 April 2025;
Published online: 22 May 2025

References

1. Kim, Y. & Zhao, X. Magnetic soft materials and robots. *Chem. Rev.* **122**, 5317–5364 (2022).
2. Yang, Z., Yang, H., Cao, Y., Cui, Y. & Zhang, L. Magnetically actuated continuum medical robots: a review. *Adv. Intell. Syst*. **5**, 2200416 (2023).
3. Du, X. & Yu, J. Image-integrated magnetic actuation systems for localization and remote actuation of medical miniature robots: a survey. *IEEE Trans. Robot.* **39**, 2549–2568 (2023).
4. Kim, Y. et al. Telerobotic neurovascular interventions with magnetic manipulation. *Sci. Robot.* **7**, eabg9907 (2022).
5. Pittiglio, G. et al. Patient-specific magnetic catheters for atraumatic autonomous endoscopy. *Soft Robot.* **9**, 1120–1133 (2022).
6. Richter, M. et al. Magnetic soft helical manipulators with local dipole interactions for flexibility and forces. *Soft Robot.* **10**, 647–659 (2023).
7. Dreyfus, R. et al. Dexterous helical magnetic robot for improved endovascular access. *Sci. Robot.* **9**, eadh0298 (2024).
8. Yang, Z. & Zhang, L. Magnetic actuation systems for miniature robots: a review. *Adv. Intell. Syst.* **2**, 2000082 (2020).
9. Kladko, D. V. & Vinogradov, V. V. Magnetosurgery: principles, design, and applications. *Smart. Mater. Med.* **5**, 24–35 (2024).
10. Nelson, B. J. An electromagnetic robot for navigating medical devices. *Nat. Rev. Bioeng*. **2**, 370–371 (2024).
11. Gervasoni, S. et al. A human-scale clinically ready electromagnetic navigation system for magnetically responsive biomaterials and medical devices. *Adv. Mater.* **36**, 2310701 (2024).
12. Richter, M., Venkiteswaran, V. K., de Vries, J.-P. & Misra, S. Apollo: advanced magnetic probes for minimally invasive endovascular interventions. *Eur. Heart J.* **45**, 2589–2591 (2024).
13. Obstein, K. et al. The magnetic flexible endoscope: Phase 1 first-in-human trial. *Gastrointest. Endosc.* **99**, AB581 (2024).
14. Edelmann, J., Petruska, A. J. & Nelson, B. J. Magnetic control of continuum devices. *Int. J. Rob. Res.* **36**, 68–85 (2017).
15. Lussi, J. et al. Magnetically guided laser surgery for the treatment of twin-to-twin transfusion syndrome. *Adv. Intell. Syst.* **4**, 2200182 (2022).
16. Sikorski, J., Denasi, A., Bucchi, G., Scheggi, S. & Misra, S. Vision-based 3-D control of magnetically actuated catheter using bigmag—an array of mobile electromagnetic coils. *IEEE ASME Trans. Mechatron.* **24**, 505–516 (2019).
17. Laulicht, B., Gidmark, N. J., Tripathi, A. & Mathiowitz, E. Localization of magnetic pills. *Proc. Natl. Acad. Sci. USA* **108**, 2252–2257 (2011).
18. Hwang, J. et al. An electromagnetically controllable microrobotic interventional system for targeted, real-time cardiovascular intervention. *Adv. Healthc. Mater.* **11**, 2102529 (2022).
19. Hong, A., Petruska, A. J., Zemmar, A. & Nelson, B. J. Magnetic control of a flexible needle in neurosurgery. *IEEE Trans. Biomed. Eng.* **68**, 616–627 (2020).
20. Dreyfus, R., Boehler, Q., Chautems, C. & Nelson, B. A navigation console to steer magnetic instruments under radiological guidance for neuro-vascular interventions. In *Proc. 14th Hamlyn Symposium on Medical Robotics 2022* 79–80 (The Hamlyn Centre, Imperial College London, 2022).
21. Tognarelli, S. et al. Magnetic propulsion and ultrasound tracking of endovascular devices. *J. Robot. Surg.* **6**, 5–12 (2012).
22. Heunis, C. M., Wotte, Y. P., Sikorski, J., Furtado, G. P. & Misra, S. The armm system-autonomous steering of magnetically-actuated catheters: towards endovascular applications. *IEEE Robot. Autom. Lett.* **5**, 705–712 (2020).
23. Suligoj, F., Heunis, C. M., Sikorski, J. & Misra, S. Robust–an autonomous robotic ultrasound system for medical imaging. *IEEE Access* **9**, 67456–67465 (2021).
24. Li, Z. et al. Design and hierarchical control of a homocentric variable stiffness magnetic catheter for multi-arm robotic ultrasound-assisted coronary intervention. *IEEE Trans. Robot*. **40**, 2306–2326 (2024).
25. Erin, O., Boyvat, M., Tiryaki, M. E., Phelan, M. & Sitti, M. Magnetic resonance imaging system-driven medical robotics. *Adv. Intell. Syst.* **2**, 1900110 (2020).
26. Mutlu, S., Yasa, O., Erin, O. & Sitti, M. Magnetic resonance imaging-compatible optically powered miniature wireless modular Lorentz force actuators. *Adv. Sci.* **8**, 2002948 (2021).
27. Phelan III, M. F., Tiryaki, M. E., Lazovic, J., Gilbert, H. & Sitti, M. Heat-mitigated design and Lorentz force-based steering of an MRI-driven microcatheter toward minimally invasive surgery. *Adv. Sci.* **9**, 2105352 (2022).
28. Aziz, A. et al. Medical imaging of microrobots: toward in vivo applications. *ACS Nano* **14**, 10865–10893 (2020).
29. Carpi, F. & Pappone, C. Stereotaxis niobe® magnetic navigation system for endocardial catheter ablation and gastrointestinal capsule endoscopy. *Expert Rev. Med. Devices* **6**, 487–498 (2009).
30. von Arx, D. et al. Simultaneous localization and actuation using electromagnetic navigation systems. *IEEE Trans. Robot.* **40**, 1292–1308 (2023).

31. Son, D., Yim, S. & Sitti, M. A 5-D localization method for a magnetically manipulated untethered robot using a 2-D array of hall-effect sensors. *IEEE ASME Trans. Mechatron.* **21**, 708–716 (2015).
32. Popek, K. M., Mahoney, A. W. & Abbott, J. J. Localization method for a magnetic capsule endoscope propelled by a rotating magnetic dipole field. In *Proc. 2013 IEEE International Conference on Robotics and Automation* 5348–5353 (IEEE, 2013).
33. Taddese, A. Z. et al. Enhanced real-time pose estimation for closed-loop robotic manipulation of magnetically actuated capsule endoscopes. *Int. J. Rob. Res.* **37**, 890–911 (2018).
34. Rivkin, B. et al. Electronically integrated microcatheters based on self-assembling polymer films. *Sci. Adv.* **7**, eabl5408 (2021).
35. Gleich, B., Schmale, I., Nielsen, T. & Rahmer, J. Miniature magneto-mechanical resonators for wireless tracking and sensing. *Science* **380**, 966–971 (2023).
36. Fischer, F., Gletter, C., Jeong, M. & Qiu, T. Magneto-oscillatory localization for small-scale robots. *NPJ Robot.* **2**, 1 (2024).
37. Yim, S. & Sitti, M. 3-D localization method for a magnetically actuated soft capsule endoscope and its applications. *IEEE Trans. Robot.* **29**, 1139–1151 (2013).
38. Popek, K. M., Schmid, T. & Abbott, J. J. Six-degree-of-freedom localization of an untethered magnetic capsule using a single rotating magnetic dipole. *IEEE Robot. Autom. Lett.* **2**, 305–312 (2016).
39. Norton, J. C. et al. Intelligent magnetic manipulation for gastrointestinal ultrasound. *Sci. Robot.* **4**, eaav7725 (2019).
40. Sharma, S. et al. Wireless 3D surgical navigation and tracking system with 100μm accuracy using magnetic-field gradient-based localization. *IEEE Trans. Med. Imaging* **40**, 2066–2079 (2021).
41. Xu, Y., Li, K., Zhao, Z. & Meng, M. Q.-H. A novel system for closed-loop simultaneous magnetic actuation and localization of WCE based on external sensors and rotating actuation. *IEEE Trans. Autom. Sci. Eng* **18**, 1640–1652 (2020).
42. Xu, Y., Li, K., Zhao, Z. & Meng, M. Q.-H. Adaptive simultaneous magnetic actuation and localization for WCE in a tubular environment. *IEEE Trans. Robot.* **38**, 2812–2826 (2022).
43. Zhang, M., Yang, L., Zhang, C., Yang, Z. & Zhang, L. Simultaneous actuation and localization of magnetic robots using mobile coils and eye-in-hand hall-effect sensors. In *Proc. 2021 IEEE/RSJ International Conference on Intelligent Robots and Systems* 8515–8521 (IEEE, 2021).
44. Paperno, E., Sasada, I. & Leonovich, E. A new method for magnetic position and orientation tracking. *IEEE Trans. Magn.* **37**, 1938–1940 (2001).
45. Makarov, D., Melzer, M., Karnaushenko, D. & Schmidt, O. G. Shapeable magnetoelectronics. *Appl. Phys. Lett*. **3**, 011101 (2016).
46. Assadsangabi, B., Tee, M. & Takahata, K. Ferrofluid-assisted levitation mechanism for micromotor applications. In *Proc. 2013 Transducers & Eurosensors XXVII: The 17th International Conference on Solid-State Sensors, Actuators and Microsystems (TRANSDUCERS & EUROSENSORS XXVII)* 2720–2723 (IEEE, 2013).
47. Assadsangabi, B., Tee, M. H., Wu, S. & Takahata, K. Catheter-based microrotary motor enabled by ferrofluid for microendoscope applications. *J. Microelectromech. Syst.* **25**, 542–548 (2016).
48. Jayhooni, S. M. H., Assadsangabi, B. & Takahata, K. A stepping micromotor based on ferrofluid bearing for side-viewing microendoscope applications. *Sens. Actuator A Phys.* **269**, 258–268 (2018).
49. Bandorf, R. et al. Different carbon based thin films and their microtribological behaviour in MEMS applications. *Surf. Coat. Technol.* **200**, 1777–1782 (2005).
50. Wang, T. et al. Development of a high-speed synchronous micro motor and its application in intravascular imaging. *Sens. Actuator A Phys.* **218**, 60–68 (2014).
51. Ghalichechian, N., Modafe, A., Beyaz, M. I. & Ghodssi, R. Design, fabrication, and characterization of a rotary micromotor supported on microball bearings. *J. Microelectromech. Syst.* **17**, 632–642 (2008).
52. Chautems, C. & Nelson, B. J. The tethered magnet: force and 5-DOF pose control for cardiac ablation. In *Proc. IEEE International Conference on Robotics and Automation*. 4837–4842 (IEEE, 2017).
53. Chautems, C. et al. Magnetic continuum device with variable stiffness for minimally invasive surgery. *Adv. Intell. Syst.* **2**, 1900086 (2020).
54. Richter, M. et al. Locally addressable energy efficient actuation of magnetic soft actuator array systems. *Adv. Sci*. **10**, e2302077 (2023).
55. Petruska, A. J. & Abbott, J. J. Optimal permanent-magnet geometries for dipole field approximation. *IEEE Trans. Magn.* **49**, 811–819 (2012).
56. Calin, M.-D. & Helerea, E. Temperature influence on magnetic characteristics of NdFeB permanent magnets. In *Proc. 2011 7th International Symposium on Advanced Topics in Electrical Engineering* 1–6 (IEEE, 2011).
57. Kuhn, H., Hughes, W. & Gaylord, E. Measurements of the viscosity of liquid wood's metal. *Br. J. Appl. Phys.* **13**, 527 (1962).
58. Zhang, X., Liu, J. & Deng, Z. Bismuth-based liquid metals: advances, applications, and prospects. *Mater. Horiz.* **11**, 1369–1394 (2024).
59. Mattmann, M. et al. Thermoset shape memory polymer variable stiffness 4D robotic catheters. *Adv. Sci.* **9**, 2103277 (2022).
60. Popek, K. M., Hermans, T. & Abbott, J. J. First demonstration of simultaneous localization and propulsion of a magnetic capsule in a lumen using a single rotating magnet. In *Proc. 2017 IEEE International Conference on Robotics and Automation* 1154–1160 (IEEE, 2017).
61. Sperry, A. J., Christensen, J. J. & Abbott, J. J. Six-degree-of-freedom localization with a 3-axis accelerometer and a 2-axis magnetometer for magnetic capsule endoscopy. *IEEE Robot. Autom. Lett.* **7**, 2110–2115 (2022).
62. Shen, Y., Dong, S., Liu, D., Zhang, K. & Wang, H. Active 6-DOF electromagnetic pose tracking using orientation control of the magnetic source. In *Proc. IEEE ROBIO* 1–7 (IEEE, 2023).
63. Valdastri, P. et al. A novel magnetic actuation system for miniature swimming robots. *IEEE Trans. Robot.* **27**, 769–779 (2011).
64. Ligtenberg, L.-J. W. et al. Ex vivo validation of magnetically actuated intravascular untethered robots in a clinical setting. *Comms. Eng.* **3**, 68 (2024).
65. Hou, Y. et al. A review on microrobots driven by optical and magnetic fields. *Lab Chip* **23**, 848–868 (2023).
66. Ebrahimi, N. et al. Magnetic actuation methods in bio/soft robotics. *Adv. Funct. Mater.* **31**, 2005137 (2021).
67. Khan, S. R., Pavuluri, S. K., Cummins, G. & Desmulliez, M. P. Wireless power transfer techniques for implantable medical devices: a review. *Sensors* **20**, 3487 (2020).
68. Qian, Y. et al. Advances in electrical and magnetic stimulation on nerve regeneration. *Regen. Med.* **14**, 969–979 (2019).
69. Zhang, E. et al. Dynamic magnetic fields remote-control apoptosis via nanoparticle rotation. *ACS Nano* **8**, 3192–3201 (2014).
70. Choi, J. et al. Magnetically enhanced intracellular uptake of superparamagnetic iron oxide nanoparticles for antitumor therapy. *ACS Nano* **17**, 15857–15870 (2023).
71. Aghayan, A. fit_ellipse. https://www.mathworks.com/matlabcentral/fileexchange/3215-fit_ellipse, MATLAB Central File Exchange, Retrieved June 20, 2024 (2003).
72. Aghayan, A. Amplitude and phase spectra of a signal (Fourier transform). https://www.mathworks.com/matlabcentral/fileexchange/63965-amplitude-and-phase-spectra-of-a-signal-fourier-transform, MATLAB Central File Exchange, Retrieved May 16, 2024 (2020).

Acknowledgements

This work was supported by the European Research Council (ERC) under the European Union's Horizon 2020 Research and Innovation Programme under grant 866494 Project–MAESTRO. Also, this work was financially supported in part by German Research Foundation (DFG) grant MA 5144/33-1, the European Union in the frame of project REGO (ID: 101070066), and ERC grant 3DmultiFerro (Project number: 101141331).

Author contributions

M.R. conceived and managed the project. M.R. and L.M. fabricated the synchronous motors. M.R. developed the field model and localization algorithm, and conducted the characterization and tracking experiments. P.M. and D.M. designed and fabricated the planar electromagnetic coils. All authors contributed to discussions and interpretation of results. M.R. wrote the manuscript with input from all authors. V.K.V. and D.M. supervised aspects of the research and experimental work. S.M., as principal investigator, provided overall project supervision and strategic guidance.

Competing interests

The authors declare no competing interests.

Additional information

Supplementary information The online version contains supplementary material available at https://doi.org/10.1038/s44172-025-00424-3.

Correspondence and requests for materials should be addressed to Denys Makarov or Sarthak Misra.

Peer review information *Communications Engineering* thanks Heng Wang and the other, anonymous, reviewers for their contribution to the peer review of this work. Primary Handling Editors: [Miranda Vinay and Rosamund Daw]. Peer reviewer reports are available.